Zr-in-rutile resetting in aluminosilicate bearing ultra-high temperature granulites: Refining the record of cooling and hydration in the Napier Complex, Antarctica

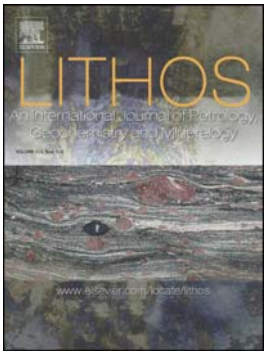

Zr-in-rutile resetting in aluminosilicate ultra-high temperature granulites: refining the record of cooling and hydration in the Napier Complex, Antarctica

Ruairidh J. Mitchell, Simon L. Harley

PII: S0024-4937(16)30425-X
DOI: doi: 10.1016/j.lithos.2016.11.027
Reference: LITHOS 4161

To appear in: *LITHOS*

Received date: 5 August 2016
Accepted date: 28 November 2016

Please cite this article as: Mitchell, Ruairidh J., Harley, Simon L., Zr-in-rutile resetting in aluminosilicate ultra-high temperature granulites: refining the record of cooling and hydration in the Napier Complex, Antarctica, *LITHOS* (2016), doi: 10.1016/j.lithos.2016.11.027

Zr-in-rutile resetting in aluminosilicate ultra-high temperature granulites: refining the record of cooling and hydration in the Napier Complex, Antarctica

Ruairidh J. Mitchell[a, 1*], Simon L. Harley[a]

[a] School of Geosciences, University of Edinburgh, The King's Buildings, James Hutton Road, Edinburgh, UK EH9 3FE

*corresponding author: ruairidhjmitchell@gmail.com

[1]Present address: Department of Applied Geology, Curtin University, GPO Box U1987, Perth, WA 6845, Australia

ABSTRACT

The relative validity and closure temperature of the Zr-in-rutile thermometer for recording UHT metamorphism is process dependent and hotly debated. We present an integrated petrological approach to Zr-in-rutile thermometry including phase equilibrium (pseudoseciton) modelling in complex chemical systems with updated mineral a-X models and systematic in-situ microanalysis of rutile. This study is centred on high-pressure rutile bearing UHT granulites from Mt Charles, Napier Complex, Antarctica. P-T phase equilibrium modelling of two garnet bearing granulites (samples 49677, 49701) constrains an overall post-peak near isobaric cooling (IBC) evolution for the Napier Complex at Mt Charles; from ~14kbar, 1100^{o}C with moderate decompression to ~11kbar, 800-900^{o}C. Local hydration on cooling over this temperature range is recorded in a kyanite bearing granulite (sample 49688) with an inferred injection of aqueous fluid equivalent to up to 9 mol% H_2O from T-MH_2O modelling. Further late stage cooling to <740^{o}C is recorded by voluminous retrograde mica growth and partial preservation of a ky-pl-kfs-bt-liq bearing equilibrium assemblage. Overall, Zr-in-rutile temperatures at 11kbar (Tomkins et al., 2007) are reset to between 606^{o}C and 780^{o}C across all samples, with flat core-rim Zr concentration profiles in all rutiles. However, zircon precipitates as inclusions, needle exsolutions, or rods along rutile grain boundaries are recrystallised from rutiles in qz/fsp domains. Reintegrating the Zr-in-rutile concentration 'lost' via the recrystallization of these zircon precipitates (e.g. Pape et al., 2016) can recover maximum concentrations of up to ~2.2wt% and thus maximum peak temperatures of ~1149^{o}C at 11kbar. Rutile Nb-Ta signatures and rounded rutile grains without zircon precipitates in hydrated mica domains in sample 49688 provides evidence for fluid-mediated mobility of Zr and Nb during retrograde cooling in hydrated lithologies. Aqueous fluid supplemented excess H_2O liberated by melt crystallisation, interacting with rutile on cooling of sample 49688 to reset Zr-in-rutile temperatures (606-780^{o}C) at the Mt Charles locality. The wide range of geochemical and petrological characteristics of Napier Complex rutile highlights that Zr-in-rutile reintegration and a broad petrological approach is required for successful interpretation of Zr-in-rutile geothermometry for long-lived regional UHT metamorphism.

Keywords: UHT metamorphism, granulites, Zr-in-rutile geothermometry, phase equilibrium modelling, fluid-rock interaction, Napier Complex

INTRODUCTION

Characterising and recording UHT metamorphism

Ultra-high temperature (UHT) metamorphism is defined as granulite facies metamorphism that achieves peak temperatures in excess of 900^{o}C (Harley, 1998; Kelsey, 2008), and represents the most thermally extreme regional-scale crustal metamorphism. UHT metamorphism has occurred at various times from the Archean to the Miocene (Brown, 2007; Pownall et al., 2014) and the P-T evolutions of UHT granulite terranes have been characterised by synoptic studies (e.g. Harley, 1989, 1998, 2004; Kelsey 2008; Kelsey and Hand, 2015). The granulite rock record displays two characteristic end-member P-T evolutions for UHT granulites: near isobaric cooling (IBC) and near isothermal decompression (ITD). However, there is dispute as to how representative this simple outcome is and the significance of metamorphic timescales associated with UHT-IBC and ITD P-T evolution.

The duration of UHT metamorphism in the lower crust has been documented for several granulite terranes (Clark et al., 2015; Kelly and Harley, 2005; Korhonen et al., 2013; Santosh et al., 2012). This is important for attributing UHT metamorphism to tectonic settings, particularly in light of evidence for secular change in orogenic style (Chardon et al., 2009, Chardon et al., 2011, Sizova et al. 2010; 2014). For example, back-arc inversion during supercontinent amalgamation has been suggested by Brown (2006; 2007) as the main tectonic setting for UHT metamorphism. Despite the occurrence of UHT granulites in recent back-arc settings as young as 19-14Ma (Osanai et al., 2006; Pownall et al., 2014), this setting cannot account for many examples of terranes where UHT conditions persist for ~40-150My (Clark et al., 2011; Harley, 2016; Kelsey and Hand 2015). These longer, high-T residence times are similar to those suggested by tectonic models of the lower crust in large, hot collisional orogens (Jamieson et al., 2010; Jamieson & Beaumont 2011). It is generally accepted that an additional heat source, e.g. from Heat Producing Element (HPE; i.e. U, Th, K) enrichment (Vila et al., 2010), is required over a >60My residence time is required to overcome the buffering of heat flow from partial melt in the lower crust in large-hot orogens (Clark et al., 2011; Stuwe, 1995).

Recording and interpreting the duration and P-T evolution of UHT metamorphic terranes has become increasingly dependent on integrating evidence from phase equilibrium modelling (Holland & Powell, 1998; 2011; Kelsey, 2008; Powell et al., 1998; Shimizu et al., 2013) with in-situ, texturally controlled accessory mineral geochronology and REE data (e.g. Kelly and Harley, 2005; Hokada and Harley, 2004; Rubatto and Hermann, 2007; Taylor et al., 2015) and geothermometry (e.g. Harley, 2016; Korhonen et al., 2013). Development of the Ti-in-zircon and Zr-in-rutile trace element geothermometers has led to many independent estimates of the temperature and duration of several UHT terranes (Harley, 2016; Jiao et al., 2011; Liu et al., 2010; Meyer, et al., 2011). Controversy has arisen, however, over the robustness of the Ti-in-zircon and Zr-in-rutile thermometers for recording UHT conditions. Conflicting evidence of their relative closure temperatures of these accessory phase thermometers (Kelsey and Hand, 2015; Harley, 2016) belies their main limitations: a dependence on petrological context, fluid-rock interaction (Luvizotto and Zack; 2007), coupled dissolution-reprecipitation (CDR) phenomena (Hayden and Watson, 2007) and deformation (Piazolo et al., 2016; Timms et al., 2011).

Granulite facies rutile varies largely in its Zr-in-rutile recorded temperature and textural context (Ewing et al., 2013; Kelsey and Hand, 2015; Harley, 2016). Flat Zr-in-rutile compositional profiles, zircon exsolution lamellae, granular exsolution and recrystallization as inclusions and along grain boundaries are common (e.g. Pape et al., 2016). Associated Zr and Si mobility within rutile grains is widely documented (Ewing et al., 2013; Taylor-Jones and Powell, 2015), and can be attributed to a number of processes. Experimental studies have constrained diffusion coefficients for Zr-in-rutile (Cherniak et al., 2007) which suggest relatively slow diffusive loss of Zr-in-rutile. However, flat core-rim Zr-in-rutile profiles are common in granulite facies rutile, and may reflect minimal diffusive loss of Zr from rutile to adjacent phases, perhaps buffered by SiO_2 concentration (Kooijman et al., 2012; Taylor-Jones and Powell, 2015). In the rutiles with reset Zr-in-rutile concentrations at lower T than compatible with the stability of its host mineral assemblage, Zr loss has been attributed to recrystallization on cooling to produce associated zircon granules (Ewing et al., 2013), while fluid mediated coupled dissolution-reprecipitation (CDR) has also been documented to facilitate accessory

phase recrystallization (e.g. Harley et al., 2007; Hayden and Watson, 2007). Initial baddeleyite exsolution before fluid-supported in-diffusion of Si along crystal defects has most recently been suggested by Pape et al. (2016) to facilitate zircon crystallisation within rutile grains. Furthermore, rutile alteration, associated Zr and Nb-Ta mobility resulting from fluid-rock interaction is also now well documented during the prograde and retrograde evolution of high-grade terranes (e.g. Luvizotto and Zack, 2009; John et al., 2011; Stepanov and Hermann, 2013). Hence, any appraisal of the Zr-in-rutile thermometer should be performed within the context of a bulk-rock lithological response to P-T evolution and associated fluid-rock processes.

In principle, by using rutile and zircon molar volumes; (Smyth and McCormick, 1995) with extensive rutile imaging and identification of Zr bearing phases associated with recrystallisation from rutile grains, it is possible to re-integrate the Zr-in-rutile concentration lost via exsolution or dissolution-reprecipitation. Previous application of this method by Pape et al. (2016) to exsolved zircon and baddeleyite has led to the recovery of peak metamorphic temperatures of ~1150^{o}C in the lower Ivrea-Verbano Zone, Italy. Whilst this is a successful application of Zr-in-rutile re-integration to a short-lived UHT thermal event without independent temperature constraints, this study of the Napier Complex provides an opportunity to test the method for long-lived UHT metamorphism and cooling with independent temperature constraints from pseudosection modelling.

Geological background

The Napier Complex of Enderby Land, east Antarctica is a late-Archaean granulite to UHT metamorphic terrane with an extensive earlier Archaean crustal history. Whilst zircon U-Pb geochronology indicates the presence of 3.60-3.85 Ga early Archaean protoliths (Black et al., 1983, 1986; Harley and Black , 1997; Kelly & Harley, 2005; Kuziak et al., 2014), the TTG orthogneisses which dominate the Napier Complex are derived from middle- to late-Archaean igneous precursors with zircon ages of ages of 3.30 Ga and 3.13-2.84 Ga (Harley and Black, 1997; Hokada et al., 2004, Horie et al., 2012; Kelly and Harley, 2005). These protoliths are

considered to pre-date a high-T / low-P metamorphic event at ca. 2.84 Ga (Harley and Black, 1997; Kelly and Harley, 2005). Orthogneisses with zircon U-Pb ages of 2.74 Ga (Horie et al., 2012) and 2.62 Ga (Carson et al., 2002) also pre-date the ubiquitous UHT tectonothermal event. Inherited detrital zircon cores limit paragneiss protolith depositional ages to >2580Ma (Horie et al. 2012) and provide a minimum upper limit of 2.58 Ga for the age of UHT metamorphism.

The P-T evolution related to UHT metamorphism in the Napier Complex has been constrained by a variety of techniques. Diagnostic mineral assemblages and conventional thermobarometers (Ellis, 1980; Harley, 1985; Harley and Motoyoshi, 2000), inverted pigeonite (Sandiford and Powell, 1986; Harley, 1987), feldspar thermometers (Hokada, 2001) and phase equilibrium modelling (Hollis and Harley, 2002; Shimizu et al. 2013) have consistently constrained peak metamorphic temperatures to >1000^{o}C. UHT metamorphic pressures of ~7-13kbar reflect a north to south gradient (Harley, 1985). This pressure gradient is represented by a transition from diagnostic lower-P osumilite + garnet assemblages in the Amundsen Bay region to higher-P orthopyroxene + aluminosilicate + feldspar bearing mineral assemblages in the Scott Mountains and Casey Bay regions (Harley and Hensen, 1990; Hokada et al., 2008; Fig. 1b). Recent phase equilibrium modelling (Shimizu et al., 2013) has inferred post-peak near-IBC at Tonagh Island at ~9kbar and by contrast, post-peak decompression at Priestley Peak from 1000-1050^{o}C at >12 kbar to 930-970^{o}C at 6.7-7.7kbar. Two neighbouring tectonic blocks with different P-T trajectories in the SW Napier complex were therefore inferred by this study. In contrast, limited post-peak decompression in the UHT part of the Napier Complex is presented by Hollis and Harley (2002) based on observations of symplectite textures replacing high-Mg garnet prior to further garnet regrowth. Early Palaeozoic K, Na and Ca metasomatism at upper-amphibolite facies (~8kbar, ~670^{o}C) conditions has been linked to post-tectonic pegmatitic intrusions that may have been produced through the underplating, at depth, of the dry granulites by previously unmetamorphosed units (Carson and Ague, 2008).

Zircon U-Pb ages coupled with zircon-garnet REE distribution evidence in anatectic leucosomes (Harley, 2016; Hokada and Harley, 2004) indicate that UHT occurred from ca. 2580 Ma to 2500-2480 Ma, consistent with the interpretation of Kelly and Harley (2005) of long-lived UHT metamorphism with a duration of >50Myr. The combination of this with Ti-in-zircon thermometry indicate that UHT conditions in excess of 900^{o}C in the Napier Complex persisted for more than 90 Myr and followed by a prolonged near-IBC evolution into the early Palaeoproterozoic (Harley, 2016). The record of anatectic zircon growth at various times in the period from 2.58 to 2.50 Ga implied that its formation was controlled by localised melt-rock interactions under UHT conditions (Harley, 2016; Kelly and Harley, 2005). Despite the strong independent evidence for prolonged UHT conditions, Zr-in-rutile temperatures so far obtained from the Napier Complex are significantly lower than the peak- and near-peak conditions, generally being in the range 740-680^{o}C (Harley, 2016; Fig. 2).

This study aims to assess the validity of Zr-in-rutile record of prolonged UHT conditions and subsequent fluid-rock interaction in the Napier Complex using four aluminosilicate bearing granulites from Mt Charles, a locality in the highest-pressure UHT region of the Napier Complex (Fig. 1). Three garnet bearing samples and an unusual Cr-rich kyanite-rutile bearing quartzite provide evidence for pressures exceeding 12kbar during the UHT event. The controls on the resetting of the Zr-in-rutile geothermometer are appraised in the light of independent P-T and T-H_2O constraints obtained from phase diagrams calculated for the UHT granulites, and the results are used to refine approaches to the use of accessory mineral thermometry in such metamorphic systems.

METHODS

Samples 49677, 49701 and 49702 are garnet-rutile bearing granulites and 49688 is a kyanite-fuchsite-rutile bearing gneiss, sampled from Mt. Charles, Enderby Land, Antarctica (Fig. 1). These four samples are subject to an integrated interpretation from petrological observation, rutile trace element analysis, Zr-in-rutile

thermometry coupled with image analysis, zircon re-integration and phase equilibrium modelling using internally consistent datasets (Holland and Powell, 1998; 2011). All mineral abbreviations are made in accordance with Whitney and Evans (2010).

Sample preparation

Samples were collected from Mt. Charles by S.L. Harley during the 1979 Australian National Antarctica Research Expedition (ANARE) to Enderby Land, Antarctica. For optical and electron microscopy and subsequent microanalysis, polished thin sections were cut perpendicular and parallel (where possible) to the main fabric. Scanning Electron Microscopy (SEM) and Electron Probe Micro-Analysis (EPMA) required carbon coating. Secondary Ion Mass Spectroscopy (SIMS) required samples to be ground to a 1-inch (25.4mm) round with a gold coating. Glass rounds and pellets of samples 49677, 49688, and 49701 were prepared for XRF bulk-rock chemical analysis.

Main phase petrography

Phase identification and characterisation of mineral textures was undertaken using transmitted light, reflected light and electron microscopy. Back Scatter Electron (BSE) images were obtained from a Carl Zeiss SIGMA FEG SEM at the Edinburgh Materials and Micro-Analysis Centre (EMMAC) facility, the University of Edinburgh. A 20keV accelerating voltage was applied with a 60µm aperture to produce slow scan speed images.

Major phase chemistry

In-situ major phase chemistry for all samples was quantified using Electron Probe Micro-Analysis (EPMA): a series of point and line analysis and X-ray element maps on a Cameca SX-100 electron microprobe at the (EMMAC) facility, the University of Edinburgh. For major elements (condition 1), a 15kV accelerating voltage was applied with a 4µm beam size and 4nA accelerating voltage. For trace elements (condition 2), a

15kV accelerating voltage was applied with a 4µm beam size and 100nA beam current. Specific protocols for spectrometer configurations are outlined in Supplementary data 1. Further in-situ major element mineral chemistry was obtained from EDS spectra from a Carl Zeiss SIGMA FEG SEM at the EMMAC facility, the University of Edinburgh, using Oxford Aztec X-ray analysis. Quantitative main phase mineral chemistry is summarised in Supplementary data 2a.

Rutile petrography and image analysis

Rutile grains and habits in all samples were observed using transmitted light, reflected light and electron microscopy. Back Scatter Electron (BSE) images were obtained from a Carl Zeiss SIGMA FEG SEM at the EMMAC facility, the University of Edinburgh. ImageJ software was used to analyse the shape, orientation and proportional surface area of zircon grains associated with rutile. '255-white' (pure white) zircon grains for further image analysis were attained by use of suitable BSE image contrast levels.

Rutile trace element analysis

In-situ spot analyses of trace element concentrations in rutile for all samples were undertaken using Secondary Ion Mass Spectrometry (SIMS) on a Cameca IMS-4f ion probe at the EMMAC facility, the University of Edinburgh (Table 1). A 5µA primary beam was applied with a 15kV impact energy, 15µm spot size and a 25µm image field, using a 4.5kV secondary ion acceleration voltage. Ion yields were calculated from the NIST 610 glass standard using GEOREM reference values. The first two out of the ten analysis cycles were discarded to reduce the effect of surface contamination. Negligible corrections for ^{54}Cr-^{54}Fe, ^{181}Ta-Ho_2O_3 overlaps were applied. Results from 4 analyses in sample 49677 (677-ru1), 8 analyses in sample 49688 (688-ru1-4) are summarised in Table 1.

Further in-situ point and line analyses of rutile trace elements were carried out using EPMA on a Cameca SX-100 electron microprobe at the EMMAC facility, the University of Edinburgh. The 20 analyses in sample

49677 (677-ru1), 22 in sample 49688 (688-ru1, 4), 2 in sample 49701 (701-ru1) and 62 in sample 49702 (702-ru1, 2) are summarised in Supplementary data 2b. An accelerating voltage of 25kV was applied with a 4μm beam size and a 200nA beam current. The following five spectrometers were set up to measure the corresponding trace element X-ray peaks: Sp1 (TAP), Nb Lα, Sp2 (LPET), Zr Lα; Sp3 (LLIF), Cr Lα, Fe Kα, Ti Kβ; Sp4 (TAP), Si Kα, Ta Kα; Sp5 (LPET), Zr Lα. The Zr Lα peak was measured over two spectrometers to allow integration over a higher count rate, therefore increasing the precision of Zr-in-rutile concentration data. Analyses with Si concentrations >400ppm were discarded, in accord with maximum Zr measurements of ~1400ppm to avoid interference from subsurface zircon inclusions. Results are summarised in Supplementary data 2b.

THEORY

Phase equilibrium modelling

P-T and T-X pseudosections were plotted using Perple_X software (Connolly and Petrini, 2010). Representative bulk rock compositions for samples 49677, 49688 and 49701 were constrained by quantitative XRF bulk rock and EPMA mineral chemistry. Complex chemical systems deemed sufficient to approach the natural behaviour of the individual samples were applied. Pseudosection models for samples 49677 and 49688 incorporated the 'hp11ver.dat' datafile based on the THERMOCALC 6.2 internally consistent thermodynamic dataset (Holland and Powell 2011). Models of 49701 utilised the 'kel04ver.dat' datafile (Kelsey et al., 2004); a modified version of the THERMOCALC 5.5 (Holland and Powell, 1998; updated 2004) internally consistent dataset required to model sapphirine equilibria with the a-X model of Taylor-Jones and Powell (2012) using Perple_X. Updated mineral a-X models for: Feldspar (Benisek et al., 2010), biotite (Tajcmanova et al., 2009), ilmenite and garnet (White et al., 2007), orthopyroxene (White et al., 2003; formulated for the dataset of Holland and Powell, 2011) and sapphirine (Taylor-Jones and Powell, 2012) were used where applicable to calculate pseudosection models.

In the kyanite-fuchsite bearing sample 49688, the exchange of chromium is a major process suggested by the presence of zoned chromite spinel and chromium-bearing mica, kyanite and rutile. However a-X mineral models for Cr in mica and kyanite have not been developed. This issue is partly circumvented by extracting the Cr-rich spinel composition (~90% of the Cr budget; based on petrographic analysis of kyanite, fuchsite and spinel) composition, as measured by electron probe analyses, from the bulk rock composition. As a result, a modified residual bulk rock composition, depleted in Cr, Fe and, to a lesser extent, Al and Mg is calculated for pseudosection modelling. The calculated pseudosection from the low-Cr modified bulk rock, can therefore be viewed as representative of the rock system for the purpose of first order interpretation. However, in this case, quantitative interpretations should be viewed with caution, as the model cannot correct for the effects of chromium in kyanite (1.77 wt% Cr_2O_3) and fuchsitic mica (1.72 wt% Cr_2O_3; Supplementary data 2a) with respect to the stability fields of Cr-absent mineral end-members. The impact of Cr on the stability of these minerals should be considered separately using suitable experiments in Cr-bearing systems.

Zr-in-rutile thermometry and reintegration

Zr-in-rutile concentrations were used to calculate metamorphic temperatures for comparison with those constrained from phase equilibrium modelling, and with previous conventional geothermobarometric estimates (Harley, 1985). The relationships relating Zr-in rutile concentration to pressure and temperature (Ferry and Watson, 2007; Tomkins et al., 2007) were applied at pressures constrained by phase equilibrium models to directly measure Zr-in-rutile temperatures recorded by rutile grains in all samples.

In a reintegration approach similar to the method recently employed by Pape et al., (2016), grain area proportions of rutile and zircon were quantified with ImageJ software and back-scatter electron (BSE) images of rutile domains. Using molar volumes of zircon and rutile, molar proportions of zircon and rutile were calculated, enabling quantitative estimation of Zr-in-rutile concentrations ‘lost’ to recrystallized adjacent zircon. Zr concentration from zircons included and in direct contact with rutile were added to representative SIMS and EPMA Zr-in-rutile concentrations obtained directly from rutiles to recover the maximum

concentration and temperature (Tomkins et al., 2007) at a pressure constrained from pseudosection models (Table 2). The lamellar geometry of zircon exsolution produced in experimental conditions along the {100} and {110} rutile cleavages (Tomkins et al., 2007; Fig. 2a) imply that area proportions of zircon and rutile may be representative of their volume proportions. Therefore, the areas of phases imaged is assumed to be representative of volume if the exsolution of zircon occurs randomly along cleavage planes in tetragonal rutile (Fig. 7a) ; the limitations associated with this assumption are discussed later (see *limitations*). Results across 4 rutiles in sample 49677 (677-ru1-3), 7 rutiles in sample 49688 (688-ru1, 4-9) and two rutiles in sample 49701 (702-ru1, 2) are summarised in Table 2.

RESULTS

Garnet-Sillimanite-Quartz-Rutile granulites 49677 and 49702

Major phase petrography and chemistry

Sample 49677 contains porphyroblastic garnet, sillimanite and late stage biotite in a ribbon quartz fabric with accessory rutile, zircon and monazite (Fig. 3). Compound garnet poikiloblasts preserve relict syn-kinematic sillimanite inclusions. Inclusions of zircon, monazite, rutile and resorbed quartz are also present in large (~1cm) garnet porphyroblasts. Prismatic sillimanite is intergrown with and mantles garnet rims. Coarse (~2mm) granoblastic quartz grains contain rutile needles arranged in three orientations. Zircon and monazite grains (up to ~200μm) occur both independently in the quartz matrix and adjacent to garnet porphyroblasts. Garnets are homogenous with respect to major element chemistry, with XMg~0.530 and XGrs~0.016 (Supplementary data 2a).

Sample 49702 is a graphite-bearing garnet-sillimanite-feldspar-quartz-rutile gneiss, with minor spinel and ilmenite (Fig. 3). Large ~1cm garnet porphyroblasts contain several generations of inclusions. Small fluid, zircon, spinel, quartz and rutile inclusions are present in discrete zones in these poikioblastic grains, while

relict syn-kinematic sillimanite inclusions and resorbed ~0.5mm quartz and rutile grains are widely observed around garnet rims. Euhedral sillimanite aggregates accompanied by abundant graphite mantles garnet porphyroblasts. Ribbon quartz and microcrystalline feldspar exist around garnet and sillimanite porphyroblasts. Large rutile grains (~500µm) and minor ilmenite occur as isolated grains in the quartz matrix. Minor late stage biotite occurs along quartz grain boundaries. Minor variations in XMg=0.513-0.538 and Xgrs=0.013-0.040 (Supplementary data 2a) are observed in garnet, however the variations do not vary systematically with garnet texture or position in the garnet grain.

Rutile petrography, trace elements and thermometry

Sample 49677 preserves coarse ~200µm euhedral rutile grains around garnet prophyroblasts (Fig. 4a), which exhibit little internal variation. Secondary rutile occurs as <1µm trails along sillimanite-quartz grain boundaries and garnet cracks. Smaller, elongate euhedral rutile grains occur in the ribbon-quartz matrix and have subhedral associated zircon precipitates as inclusions and along grain boundaries. Zircon grain habits vary from isolated, round and altered grains in the quartz fabric to interstitial subhedral grains with garnet, to granules and rims texturally associated with recrystallization from rutile. Zircon precipitates are often associated with fine orientated cracks inferred to reflect volume change from precipitating higher molar volume zircon inside rutile (Fig. 4b, 9a).

Accessory rutile in 49702 occurs in two main habits. Rutile grains adjacent to garnet, quartz and sillimanite aggregates are euhedral, internally homogenous and have minimal zircon precipitates as granules along grain boundaries. Conversely, rutile grains isolated in the quartz fabric are euhedral and often display large ~50µm rounded zircon precipitates on grain boundaries, and late stage zircon along cracks within the rutile.

Trace elements in rutile in sample 49677 have been determined from 20 EPMA (Supplementary data 2b) and 4 SIMS (Table 1) analyses. Zr-in-rutile concentrations are variable (Fig. 9b(i), Table 1; 510-1402ppm). An

EPMA line analysis of a rutile adjacent to garnet and quartz yields a near-flat Zr-in-rutile rim-to-rim profile (510-643ppm) corresponding to Zr-in-rutile temperatures of between 675-696°C at 11kbar (Tomkins et al., 2007). Adjacent rutile grains in the same petrological setting preserve higher Zr-in-rutile concentrations of 1260-1402ppm, corresponding to 756-780°C Zr-in-rutile temperatures (Table 1). Nb/Ta ratios in all analysed rutile grains fall between 13.7 and 20.7 and there are no systematic internal chemical variations within rutile grains adjacent to garnet in sample 49677 (Fig. 9b(i)). Whilst Fe concentration appears to increase towards adjacent garnet, this may be due to X-ray fluorescence effects.

Seven SIMS (Table 1) and 62 EPMA (Supplementary data 2b) analyses have been obtained in two rutile grains in sample 49702. One grain is in contact with a garnet porphyroblast and the other is isolated in the quartz fabric (Figure 9, Table 1). The rutile grain adjacent to garnet records Zr-in-rutile concentrations of 244-254ppm resulting in calculated temperatures of 615-618°C at 11kbar (Tomkins et al., 2007), while larger ~400µm rutiles isolated in the quartz matrix have flat Zr-in-rutile core-rim profiles and Zr-in-rutile concentrations between 727 and 943ppm, giving temperatures of 699-746°C at 11kbar (Fig. 9b(ii), Table 1). Nb/Ta ratios in 49702 rutiles vary between 7.52 and 13.09. Rutile grains adjacent to garnet have an elevated V concentration ~3700ppm, compared with those isolated in quartz (~2600ppm). There are significant internal variations in Ta and an abrupt increase in Si concentration towards the rutile rim potentially related to grain edge effects and secondary fluorescence from the adjacent quartz in high beam current EPMA analyses.

Re-integration of exsolved zircon into rutile in 49677 yields two temperature estimates that depend on the textural context of rutile. Rutile in garnet-quartz domains contain relatively few zircon needles and granules leading to re-integrated Zr-in-rutile concentrations of 1614ppm and 1040ppm and therefore temperatures of less than 780°C at 11kbar. Rutile isolated in the quartz matrix contain voluminous zircon inclusions and precipitates, the reintegration of which recovers Zr-in-rutile concentrations of 13954ppm (1.4 wt% Zr), resulting in Tomkins et al. (2007) temperatures of 1068°C at 11kbar (Fig. 4b; Table 2). Re-integrated Zr-in-

rutile temperatures in sample 49702 for rutile grains isolated in quartz are 965°C at 11kbar (Tomkins et al., 2007; Zr-in-rutile = 7258ppm), while rutile adjacent to garnet yields 874°C (Table 2).

Phase equilibrium modelling

Phase equilibrium modelling of 49677 was undertaken in the NCKFMASHTO chemical system (Fig. 6a). H_2O proportions were determined from modal proportions of retrograde biotite (≈ 0.5 wt% H_2O), the only hydrous phase present in the sample after post-peak melt crystallisation. This H_2O content should be viewed as a maximum, accounting for potential post-peak hydration and melt re-integration, and not necessarily representative of H_2O contents at peak UHT conditions. However, high modal melt at peak conditions from relatively high H_2O contents cannot be ruled out due to a lack of preserved gneissic layering. The O_2 (XFe^{3+}) molar proportion was determined from a calculated T-XO_2 plot which indicated that a rutile bearing, ilmenite absent peak metamorphic assemblage, as observed petrologically, can only be present at $XO_2 \approx 0$.

The solidus for 49677 is near vertical at ~810°C. Ilmenite stability calculated with new a-X models incorporating Ti and Fe^{3+} (White et al., 2007) is limited to below 7kbar at >700°C in this bulk-rock composition. Sapphirine is absent even at extreme temperatures >1000°C due to the low XFe^{3+}, moderate bulk XMg and high S/SAFM = 0.79. The liq-grt-sil-qz-rt peak assemblage is constrained to a P-T field at >900°C and >9kbar. Garnet Xgrs and XMg isopleths in liq-grt-sil-qz-rt±H_2O±bt bearing fields are near vertical so cannot constrain metamorphic pressure above the minimum of 9kbar, however Xgrs = 0.14 places peak metamorphic conditions at ~1000°C (at 11-12kbar). The maximum modal melt volumes at these peak metamorophic conditions reach ~14-16 vol% (Supplementary data 4). Reset XMg = 0.53-0.54 and the formation of small modal proportions of late stage biotite is consistent with a near IBC P-T evolution to ~850°C at 11kbar (Fig. 6c).

Garnet-Spinel-Corundum-Sillimanite-feldspar-ilmenite-rutile granulite 49701

Major phase petrography and chemistry

49701 has a quartz absent assemblage with high (~40% volume) modal proportions of porphyroblastic garnet (Fig. 5a). Spinel and corundum intergrowths are widespread, and coarse antiperthite feldspar domains with porphyroblastic spinel and sillimanite occur (Fig. 5b, c). Garnet consists of primary porphyroblasts (grt1) with discrete secondary overgrowths (grt2). Secondary garnet coexists with corundum, spinel, rutile and plagioclase present in adjacent intergrowths. Corundum occurs exclusively as interstitial grains in primary and secondary garnet. Sillimanite porphyroblasts are synchronous with secondary garnet growths and are associated with rutile and ilmenite. Minor, texturally late-stage biotite is present in some micro-domains (Figure 5d). Accessory rutile is present in grt2 intergrowths and on garnet-feldspar grain boundaries, whilst ilmenite occurs in association with grt2 and mantles sillimanite porphyroblasts. Primary and secondary garnet grains are homogenous in their major element compositions, with a low XMg = 0.34-0.38 and Xgrs 0.05-0.06 reflecting the XMg poor bulk rock composition. Spinel compositions are XMg = 0.328-0.419, Xghn (gahnite) = 0.080-0.087 and Xchr = 0.057-0.096 (Supplementary data 2a).

Rutile petrography, trace elements and thermometry

Rutile grains in sample 49701 occur in association with secondary garnet and adjacent to corundum, ilmenite and spinel. Altered rutile grains occur with sillimanite between secondary garnet and the meso/antiperthite feldspar matrix. Absence of rutile inclusions or interstitial rutile in association with primary garnet porphyroblasts indicates that rutile growth occurred after primary garnet formation (at or after peak metamorphic conditions), potentially synchronous with sillimanite and secondary garnet. Rutile is internally homogenous and lacking zircon needles, granule precipitates or rinds.

Rutile trace elements in sample 49701 are constrained from 2 SIMS (Table 1) and 2 EPMA point analyses (Supplementary data 2b). Nb/Ta ratios are between 15.7 (SIMS) and 19.0 (EPMA), 3094-3424ppm Cr and 5089-5261ppm V. Zr-in-rutile concentrations vary between and 730 and 1184ppm, leading to Zr-in-rutile

temperatures between 704°C and 744°C at 11 kbar (Tomkins et al., 2007). A lack of zircon needles, granules or rinds associated with rutile in 49701 means that Zr re-integration is not warranted.

Phase equilibrium modelling

A P-T pseudosection for a representative bulk rock composition for 49701 was drawn in the MnNCKFMASHTO chemical system (Fig. 6b). Low modal percentages of retrograde biotite, the only hydrous phase present, limits H_2O proportions to 0.53 mol%. From exploratory T-XO_2 pseudosections, rutile bearing assemblages at ~11kbar are limited to compositions with <0.04 mol% O_2. Sapphirine is restricted to T > 1000°C by the low XO_2 and low bulk-rock XMg. As the bulk rock composition is SiO_2 undersaturated, corundum bearing assemblages dominate high pressure assemblages and the quartz-absent solidus is at approximately 900°C. Importantly, rutile is present only along the retrograde P-T path in this rock, ilmenite is the main Ti-bearing phase at peak conditions. This is reflected by the petrographic association of rutile in direct contact with ilmenite along with secondary garnet. This interpretation post-peak rutile crystallisation is further reflected by low absolute Zr-in-rutile concentrations and lack of exsolved zircon within rutile grains in this sample. The accuracy of isopleths for garnet Xgrs and Xpy in the MnNCKFMASTO chemical system is limited by the presence of complex quarternary spinel (Fe-Mg-Cr-Zn); Xghn (gahnite) = 0.0800-0.0870 and XCr = 0.0570-0.0960. Consequently, the Fe-Mg exchange between garnet and spinel cannot be represented precisely in this pseudosection.

The P-T evolution compatible with mineral textures observed in sample 49701 is initially close to UHT-IBC and then may involve moderate decompression accompanying significant cooling. This results in an overall post-UHT dP/dT gradient of approximately 11-12 bar/°C over the PT interval from ~14.5kbar, >1100°C to 11kbar, 850°C. A peak liq–pl-spl-grt-ilm-crn assemblage is implied by Fe-Mg-Zn-Cr spl and crn inclusions in grt1, with plagioclase (without associated k-feldspar) formed between grt1 and grt2, and slightly elevated garnet Xgrs = 0.05-0.06 compositions. Modal melt volume at peak metamorphic conditions range between 8-12 vol% (Supplementary data 4). Synchronous growth of pl, kfs, ilm, rt and bt with grt2, followed by late

stage sil formation contemporaneous with grt2 rim growth, and garnet XMg 0.340 and 0.345 constrains the post peak evolution to ~11kbar at 800-900^{o}C (Fig. 6b).

49688 kyanite-mica-feldspar-quartz-chromite-rutile gneiss

Major phase petrography and chemistry

Granulite 49688 exhibits gneissic banding into ~1-5mm width domains that are either quartz dominated or feldspar-fuchsite dominant (Fig. 7a).

Quartz dominated domains preserve ribbon textured quartz which contain abundant rutile needles often >20µm in length and linear zones of fluid inclusions. Euhedral accessory rutile (up to ~250µm) is common (Fig. 7d). Grain boundary migration is displayed between early, high-T ribbon quartz and the recrystallized quartz that bounds feldspar-fuchsite domains. Quartz-feldspar and feldspar-mica grain boundaries are lobate and low angle. Resorbed feldspar near quartz grain boundaries (Fig. 7c) suggests the former presence of partial melt, trapped in microdomains between quartz and feldspar (e.g. Sawyer, 1999; Vernon, 1999; 2011).

Feldspar-fuchsite domains are texturally complex. Their margins with quartz domains consist of plagioclase and minor K-feldspar. The majority of the K-feldspar is replaced by two generations of mica: phengitic mica near domain margins and fuchsitic mica at the centre of domains. Blue pleochroic kyanite porphyroblasts occur exclusively in feldspar-fuchsite domains. Kyanite porphyroblasts are extensively altered and resorbed, and have spongey-textured intergrowths with mica and quartz (Fig. 7b). Chromium-rich spinel (chromite) displays skeletal intergrowths with fuchsite and is always mantled by a mica corona. Rounded, altered rutile and minor, highly altered pyrite occur in the fuchsite mica domains. Biotite is preserved in association with kyanite or included in kyanite, and is present with <1% volume modal abundance in fuchsite domains, often on chromite.

Local, partial preservation of altered kyanite, associated biotite and curviplanar qz-fsp partial melt textures (Fig. 7e) implies a relict liq-ky-kfs-pl-bt-qz-rt equilibrium assemblage overprinted by retrograde fuchsitic mica. Chromium is a significant chemical component in kyanite (X_{Ky}^{Cr} = 0.017-0.019), fuchsite (0.041-0.050 XCr), chromite spinel (Xchr 0.44-0.52; Supplementary data 2a) and rutile (~1wt%; Table 1). Chromium zoning is present even in small (~20µm) chromite grains.

Rutile petrography, trace elements and thermometry

Rutile is present as an accessory phase in both quartz-feldspar and fuchsite dominated domains, occuring in contrasting habits. In fuchsite-dominated domains, large 200µm rutile grains coexist with chromite and are often elongate, rounded and highly altered. Two contrasting styles of rutile-associated zircon are present; euhedral zircon exsolved along rutile cleavage, and rounded zircon granules are limited to rutile grain boundaries.

Large (>250µm), euhedral rutile grains are preserved in quartz and feldspar sub-domains which have not reacted to form mica aggregates. These rutiles preserve a large proportion of zircon precipitates in a variety of habits (Fig. 8). Zircon within rutile precipitates either as euhedral rods ~5µm in diameter aligned with rutile cleavage or as small <1µm ovoid, round inclusions (Fig. 8b, d). Several zircon 'rod' inclusions are hollow or cylindrical. The volume change associated with zircon recrystallization in rutile (up to +6.3% in 49688; Table 2) and leads to cracks within the rutile crystal, often aligned with the rutile cleavage (Fig. 9a). Rounded zircon precipitates occur along grain boundaries and in pre-existing cracks in rutile. Zircon needles ~30µm in length are exsolved throughout these large rutile grains.

Based on 22 EPMA data points (Supplementary data 2b) and 8 SIMS analyses (Table 1), rutile grains in 49688 preserve Zr-in-rutile concentrations in the range 219-383ppm, corresponding to apparent equilibrium

temperatures of 606-653°C at 11kbar (Tomkins et al., 2007). Core-rim Zr-in-rutile chemical profiles are flat in rutile grains in both quartz and fuchsite-dominated domains (Fig. 9b(iii); Table 1). Nb/Ta ratios for rutile grains in quartz domains lie between 15.7 and 29.1 for SIMS analyses and 24.8-68.0 based on more numerous EPMA analysis points (Supplementary data 2b). Nb/Ta ratios of 12.5-13.9 (SIMS) and 9.1-17.3 (EPMA) of rutile grains in fuchsite-dominated domains reflects a relative Nb depletion in these rutiles and a smaller range of Nb/Ta ratios compared to those in the quartz-dominated domains (Fig. 10).

Two Zr-in-rutile responses are therefore displayed in sample 49688. In the hydrated fuchsite-rich domains, rutile grains are rounded and altered, and any formerly higher zirconium concentration that may have been re-precipitated as zircon granules or rinds on rutile has been mobilised away from the rutile (Fig. 8e, f). In contrast, in the little-hydrated quartz-dominated and feldspar-bearing domains, zircon exsolved and precipitated from rutile is not re-mobilised from the rutile, instead is retained and preserved as relatively abundant zircon precipitates in several generations and habits (Fig. 8a-d).

Rutile grains in both habits in both the quartz-feldspar and fuchsite-dominated domains display flat core-rim Zr-in-rutile profiles leading to calculated temperatures in the range 606-653°C (Fig. 9b(iii); Table 2). However, reintegration of the Zr associated with zircon precipitated in rutiles in quartz-dominated domains give Zr-in-rutile concentrations 6796-21996ppm and corresponding maximum peak temperatures of 956-1149°C (Fig. 8a-d; Table 2; Tomkins et al., 2007). The relatively small zircon granules associated with rutile grains in fuchsite domains recover temperatures 659-742°C on reintegration (Fig. 8e, f; Table 2).

The distinctive depleted Nb signature (Fig. 10), of the low-Zr rutiles preserved in the fuchsite-dominated domain is compatible with Zr and Nb mobilisation away from rutile associated with hydration. Nb, Ta and Ti solubility in metamorphic fluids is generally limited, but has been documented to increase in the presence of Na-Al-Si or Cl and F chemical species and in supercritical fluid conditions (Rapp et al., 2009; see ***Discussion***).

Phase equilibrium modelling

As noted in the **methods** section, the composition associated with Cr-spinel has been extracted from the 49688 bulk composition in accord with the spinel modal proportion to minimise the influence of Cr on the modelled the bulk rock composition. T-MH_2O pseudosections in the NACKFMASHT chemical system for this modified version of sample 49688 are drawn for P = 11kbar (constrained from 49677 and 49701 P-T pseudosections; Fig. 6) and compositions X0 and X1 representing zero mol% H_2O and 15 mol% H_2O respectively (Fig. 11). Garnet stability is limited to MH_2O < 0.50. The solidus drops from ~800^oC to ~700^oC at 0.5 MH_2O. Kyanite vol% decreases rapidly with increasing MH_2O and decreasing temperature, from ~9% at 820^oC to 0% at ~775^oC at high MH_2O (Fig. 11b). Mica vol% increases from 0% to 41% at high MH_2O from and ~720^oC; this Cr-absent white mica has stability limited to below 815^oC (Fig. 11c).

The T-MH_2O of sample 49688 is characterised by a peak metamorphic temperature of 1000-1100^oC at 0.1-0.5 MH_2O, constrained by the absence of garnet and the presence of an aluminosilicate phase in the liq-pl-sil-qz-rt bearing peak assemblage. Cooling from UHT conditions initiates the crystallisation of biotite and then K-feldspar from melt, producing a liq-pl-ky-kfs-bt-qz-rt equilibrium assemblage which occupies a stability field at ~825-875^oC at 0.35 MH_2O to 825^oC at 0.7 MH_2O for pressures of 11 kbar.

The final range of metamorphic temperatures of 600-650^oC (from reset Zr-in-rutile; Fig. 2, Table 1) can be achieved between two end-member T-MH_2O evolutions intersecting the stability field of the liq-pl-ky-kfs-bt-qz-rt equilibrium assemblage. Scenario (i) illustrated by Fig. 11d is achieved by cooling to ~820^oC at 0.35 MH_2O. This would lead to partial melt crystallisation near the solidus at ~820^oC. H_2O loss with melt crystallisation could inhibit any minor garnet growth and preserve the liq-pl-ky-kfs-bt-qz-rt equilibrium assemblage. Finally, the preserved reaction assemblage may be formed at 600-650^oC by late-stage H_2O addition to >0.6 MH_2O, thereby avoiding garnet stability fields and overstepping melt bearing fields between ~740^oC and ~820^oC. A resultant mica-pl-qz-rt mineral assemblage with excess H_2O and local relict ~9 vol%

kyanite and K-feldspar could then evolve at ~720°C and 0.6MH_2O. From Fig. 11d, scenario (ii) depicts an earlier MH_2O increase to 0.7 on cooling from temperatures >850°C to the liq-pl-ky-kfs-bt-qz-rt equilibrium assemblage. If the high MH_2O = 0.7 content is achieved early, partial melt crystallisation and therefore H_2O liberation is delayed until 725-750°C. Scenarios (i) and (ii) depicted in Fig. 11d both can generate the mineral textures observed in 49688 but require addition of H_2O at different stages of their evolution. An open system with an episode of melt loss, leading to ~0 wt% H_2O during cooling between ~960-840°C can produce the required bt-liq-pl-kfs-ky-qz-rt equilibrium assemblage (Fig. 11d; scenario iii); however the inferred garnet stability for this scenario is inconsistent with petrological observations. A closed system – e.g. cooling with a fixed MH_2O can only generate the required equilibrium and final assemblages if the rock has a high melt content (dictated by MH_2O > 0.6) from the start of its evolution. Evidence for high vol% of retained former melt is lacking, given that the rock is strongly layered and non-migmatic, with undisrupted alternating 1-2mm quartzitic and ky-mica-fsp banding (Fig. 7a), implying that any melt accumulates at the source after mica crystallisation. Therefore scenario (i) in Fig 11d is the most likely as it entails the lowest mode of partial melt during phengitic mica crystallisation (<8 vol%), below the first melt percolation threshold (Sawyer, 1994), and consistent with resorbed fsp textures (Fig. 7c,e).

The T position of the sillimanite-kyanite reaction in Fig. 11 is 900°C, defined in a Cr-free chemical system. However, elevated $X_{Al2SiO5}^{Cr}$ increases the stability of kyanite up-temperature by 80°C at 20kbar with full Cr^{3+}=Al^{3+} substitution (Seifert and Langer, 1970). Using an ideal Cr^{3+}=Al^{3+} one site (octahedral) substitution model for Cr in kyanite and $X_{Al2SiO5}^{Cr}$=0.017 based with EPMA data (Supplementary data 2a), the kyanite-sillimanite transition occurs to 933°C at 11kbar in sample 49688 rather than 900°C, and would be close to 1000°C at 13kbar.

DISCUSSION

1. Limitations on analysis of the UHT to post-peak evolution at Mt Charles

Re-integrated Zr-in-rutile contents

The zircon-reintegration method adopted here uses ImageJ software to quantify the relative areas of zircon and rutile from slow-speed scan BSE images. The method assumes that the area proportion of rutile and zircon imaged is representative of the volume proportion of zircon and rutile. While this assumption holds for a random 3D distribution of zircon exsolution lamellae in rutile governed by cubic or tetragonal symmetry rutile (Fig. 9a), it is not necessarily true if there is clustering of recrystallized zircon through preferred precipitation along grain boundaries or cracks in rutile. The resultant uncertainty in reintegrated Zr-in-rutile concentrations can be minimised by consideration of many rutile grains. Although clustering of recrystallized zircon in rutile is commonplace in this study (Fig. 8a-d), images of 12 of rutiles over 3 samples were analysed, using two perpendicular thin sections for sample 49688. Comparable re-integrated Zr-in-rutile concentrations were returned, approaching previously inferred peak temperatures in this region of the Napier Complex (Fig. 6, 12). This provides empirical support for the re-integration method applied here.

Further limitations apply to the reintegration method. In this study, recrystallised zircon grains are pure white in BSE images and so have to be distinguished other accessory phases by petrography and in-situ X-ray spectral analysis on a FEG SEM, or by a more detailed comparison of BSE brightness. Secondly, this method assumes that zircon forming rinds on rutile is derived from the rutile grain. While this is likely for exsolved zircon rods and lamellae, some round, ovoid zircon inclusions (Fig. 8b, d) could be primary inclusions rather than exsolved/recrystallised zircon. This may be tested by in-situ analysis of zircon for trace elements (i.e. REE, U, Th), however many zircons are too small to allow conventional SIMS analysis. A further limitation is that rutile grains are assumed as pure (100% TiO_2) and the method does not account for other trace elements, i.e. ~1wt% Cr in sample 49688 rutiles; however, this limitation is relatively trivial given the other uncertainties involved with calculation of Zr-in-rutile concentration by re-integration, propagating errors of only tens of ppm in reintegrated Zr-in-rutile concentrations. Finally, the re-integrated Zr-in-rutile concentration recovered is dependent on the extent to which recrystallized zircon is preserved and successfully imaged in the rutile domain. For example, fluid-mediated mobilization of zircon from host rutile grains may decrease the apparent Zr-in-rutile concentration and temperature from reintegration.

Phase equilibrium modelling

Phase equilibrium modelling of hydration in sample 49688 is appropriate for modelling the behaviour of the adjusted bulk rock composition under equilibrium conditions. However if the system is not allowed to evolve to equilibrium at a given P-T condition then assemblages predicted by pseudosections may not be compatible with the mineral assemblages and reaction textures observed in the real sample or may not accurately represent any mineral textures not exposed to the whole rock volume. The voluminous (~40 vol%) mica overprint in sample 49688 presents such an example; there is partial preservation of disequilibrium textures with relict qz-fsp melt textures, altered kyanite and chromite in fuchsite-dominated domains (Fig. 7).

Extracting quantitative P-T-MH_2O data from pseudosection modelling is limited in Cr-bearing assemblages as internally consistent datasets and relevant mineral a-X models incorporating Cr have not been developed. Cr is a significant chemical component in sample 49688, present in fuchsitic mica, chromite, chromium kyanite and rutile. To minimise the effect of the Cr content on 49688 pseudosection models, spinel composition was eliminated from the measured bulk rock composition (constant with 90% of bulk-rock Cr in spinel) and a new adjusted bulk rock composition developed for pseudosection modelling. As a result, the pseudosection does not quantifiably represent the complete, 'real' response of sample 49688. It is therefore important to view results from pseudosection modelling of sample 49688 from a broad interpretive stance – the pseudosection does not quantifiably represent the 'real' response of complete the bulk rock composition of sample 49688 – but is useful for interpretation in conjunction with constraints from pseudosections of nearby samples and rutile thermometry.

In the quartz-absent sample 49701, garnet composition isopleths for Xpy and Xgrs are indirectly affected by the complex spinel composition. Spinel in 49701 contains Zn (Xghn (gahnite) = 0.0800-0.0870)) and XCr (chromite) = 0.0570-0.0960) components, collectively forming some 14-20 mol% of the spinel phase. As Zn and Cr are not represented in the MnNCKFMASHTO chemical system, the Fe-Mg contents, and modal abundances, of spinel are not accurately represented in the pseudosection model. The calculated garnet modes,

Xgrs and Xpy isopleths within the stability fields of spinel-garnet-bearing assemblages can therefore only broadly constrain P-T conditions. In particular, a decreased mode of garnet in comparison to spinel in the full Cr-Zn bearing system would lead to that garnet having a higher Xgrs at a given P-T than calculated in the model system. Therefore, the peak calculated metamorphic pressures of ~14kbar, and the extent of decompression accompanying UHT cooling which has been constrained using garnet Xgrs isopleths may both be lower than calculated and presented for 49701.

Pseudosection models for pelitic, melt and Zr bearing systems have been used in recent work (Kelsey and Powell, 2011) to calculate zircon and rutile mineral modes and ideal Zr-in-rutile concentrations. However, there are important limitations to consider when applying this approach to the Zr-in-rutile thermometer. As demonstrated by Pape et al. (2016) and in this study, the retention of Zr in rutile grains is texturally controlled by rutile grain morphology, the proximity of Zr bearing phases and mobility of Zr associated with fluid interaction. It may therefore be misleading to model Zr-in-rutile concentrations and mineral modes based on a bulk rock composition alone.

2. Metamorphic evolution of Mt. Charles granulites

A near-peak, peak and post-peak P-T evolution of the Napier Complex at Mt Charles from up to 14.5 kbar, 1100^{o}C to 11kbar, 800-820^{o}C is broadly constrained from pseudosection modelling of garnet bearing samples 49677 and 49701 and the maximum Zr-in-rutile concentrations obtained from zircon reintegration back into rutile, which has yielded peak metamorphic temperatures of 956-1149^{o}C (Fig. 12a, Table 2). The implied post peak UHT-IBC evolution with moderate decompression at deep crustal (11-14kbar) levels over a temperature range of ~200-300^{o}C is in broad agreement with IBC from peak conditions of ~900^{o}C and 10.6-11.0kbar at Mt Charles inferred by garnet-orthopyroxene thermometry by Harley (1985).

Recent phase equilibrium modelling of sapphirine-bearing assemblages from Priestley Peak and Tonagh Island by Shimizu et al. (2013) has been used to hypothesise the existence of two neighbouring tectonic blocks with contrasting post-peak P-T trajectories. The ~9kbar near-IBC P-T path deduced by Shimizu et al. (2013) for Tonagh Island (Fig. 12b(iii)) is consistent with previous studies (Harley, 1985; Harley and Hensen, 1990; Hollis and Harley, 2002; Hokada et al., 1999). Their P-T path involving extensive post-peak UHT-decompression from >12kbar at 1000-1050^{o}C to 6.7-7.7kbar at 930-970^{o}C at Priestley Peak (Fig 12b(iv)), however, is inconsistent with the regional P-T-t syntheses of Harley (1985) and Harley and Hensen (1990). Mt Charles is located south of the block occupied Priestley Peak, and while moderate decompression at ~11-12 bar/^{o}C is evident from the results of the present study, there is no evidence for UHT-ITD at ~43 bar/^{o}C, to pressures of 6.7-7.7 kbar at >900^{o}C (Fig. 12b). From the mineral assemblages in garnet-bearing lithologies, the minor decompression through ~2kbar from UHT conditions closely resembles that invoked by Hollis and Harley (2002) for Tonagh Island and other localities centred on Amundsen Bay (Fig 12b).

The overall deep-level post peak P-T path at 14-11kbar inferred from the Mt Charles rocks is similar to P-T histories invoked for some other UHT terranes with high-P peak conditions e.g. the Eastern Ghats Province (Korhonen et al., 2011; 2013). On the other hand, it differs from the strongly decompressional post-peak P-T paths generally associated with large-hot orogen models in which lower-crustal rocks may typically achieve UHT for some 20-25Myr before UHT-ITD (Jamieson et al., 2010; Jamieson and Beaumont, 2013; Harley, 2016). The high pressure, post peak UHT-IBC evolution inferred for Mt Charles suggests a prolonged residence time at HP-HT conditions in the lower crust, perhaps linked to the removal of a heat source through lateral flow in (e.g. Chardon et al., 2009; 2011), or the long-lived presence of a heat-flow buffer e.g. partial melt (Clark et al., 2011; Stuwe, 1995). The P-T path from pseudosection modelling and Zr-in-rutile thermometry of the Mt Charles samples can help to constrain its tectonic evolution. Further geochronological data is required to constrain the absolute timescales of peak UHT and the post peak metamorphic evolution and therefore correlate this P-T evolution with evidence from Amundsen Bay and Casey Bay (Harley, 2016). This study points to the requirement for further spatial, structural correlation and geochronological cross-

correlation to inform tectonic models for the near-peak and post-peak P-T evolution of the Napier Complex as a whole.

Cooling from 800-820^{o}C to 600-750^{o}C at 11kbar is constrained by reset Zr-in-rutile concentrations corresponding to temperatures 600-780^{o}C at 11kbar across all samples, and by the intensely hydrated mineral assemblages in sample 49688 (Fig. 2, 12; Table 1). Garnet-absent mineral equilibria in sample 49688 require the addition of H_2O to $MH_2O > 0.6$ (equivalent to 9 wt% H_2O) at some time during near-IBC P-T evolution from ~1000^{o}C to ~820^{O}C in order to achieve the observed final mica-pl-qz-ru-H_2O hydrated assemblage (Fig. 11d) and enable further Zr-in-rutile resetting; temperatures of ca.600-650^{o}C are recorded in sample 49688. As noted above, this hydration and reaction may be produced via two end-member T-MH_2O evolutions; (i) prolonged, early stage crystallisation of partial melt at $MH_2O > 0.5$ with cooling or (ii) a discrete episode of melt crystallisation at 725-750^{o}C on cooling at high MH_2O conditions developed through early H_2O addition (Fig. 11d). Realistically, any H_2O introduced into 49688 from an outside source will be supplemented by the excess H_2O liberated by crystallisation of partial melt at ~725-750^{o}C on cooling of 49688 at $MH_2O > 0.6$.

The chemistry of the low-Zr rutiles preserved in 49688 provides further evidence for the introduction of fluids. The best-fit rutile Nb/Ta ratio across all samples (131 analyses) is 13.3, close to suggested crustal sub-chondritic Nb/Ta values (Barth et al., 2000). However, the low-Zr rutiles in fuchsite-dominated domains within 49688 preserve uniquely fractionated Nb-Ta ratios (Fig. 8e, f; 10) that imply a net loss of Zr and Nb from rutile domains. Such Zr and Nb dissolution into metamorphic fluid requires high Na-Al-Si or Cl and F fluid concentrations (Rapp et al., 2009), a feature not yet observed in Napier Complex fluid inclusions (e.g. Tsunogae et al., 2002; 2008). It is possible, however, that the near-IBC P-T evolution of the Napier Complex may mitigate against preservation of brines in fluid inclusion suites. The near-IBC path, which is close to perpendicular to steep dP/dT H_2O-NaCl isochores, could facilitate brine mobility along grain boundaries through inclusion underpressurization (Touret et al., 2016). This study points to the requirement for further

fluid inclusion studies in the Napier Complex, focused on regions where late-stage shearing and hydration are evident (Newton, 1990; Touret and Huizenga, 2012; Touret et al., 2016).

In-situ geochronological data from zircon (U-Pb), monazite (U-Th-Pb) and rutile (U-Pb) in sample 49688 is required to determine the age of hydration. H_2O addition at temperatures less than ~820^{o}C may either be associated with regional D3 deformation (Harley, 1985) and Paleoproterozoic post-fabric veining in accordance with regional cooling paths constrained from mineral thermochronology (e.g. Choi et al., 2006; Suzuki et al., 2006), or with an early Palaeozoic metasomatic overprint (Carson et al., 2002; Carson and Ague, 2008). In the former case where hydration is associated with the regional cooling path, a cooling rate may be inferred from previous isotopic studies: monazite (U-Th-Pb) dates and Sm-Nd, Lu-Hf mineral isochron data (Choi et al., 2006; Kelly and Harley, 2005; Suzuki et al., 2006) and in-situ, leucosome zircon U-Pb dates and corresponding Ti-in-zircon temperatures. Linear extrapolation from these datasets shows that cooling to ~625^{o}C, indicated here by reset rutiles, could occur between.2440-2200Ma if UHT-IBC in the Napier Complex occurs uniformly across localities.

3. Implications for Zr-in-rutile thermometry

Across three garnet-sillimanite bearing granulites (49677, 49701 and 49702) and a kyanite-fuchsite-feldspar-quartz-rutile-chromite gneiss (49688), metamorphic rutile grains are preserved in a variety of petrological settings. The samples have different P-T-X stability fields for rutile, preserve different rutile trace element signatures and preserve varied Zr-in-rutile recorded temperatures. Meaningful conclusions from Zr-in-rutile thermometry therefore must be interpreted within the wider context of micro-geochemical and petrological processes.

Zircon associated with rutile, as both inclusions or ‘precipitates’ on rutile grain boundaries, have been documented for high-T metamorphic conditions (Ewing et al., 2013; Pape et al., 2016; Taylor-Jones and

Powell, 2015). Formation of zircon granules and exsolution lamellae has been attributed to Zr-in-rutile loss through recrystallization because of a lack of preserved diffusion profiles (Ewing et al., 2013; Kooijman et al., 2012; Fig. 9b), as a result of SiO_2 buffered diffusive loss of zircon (Taylor-Jones and Powell, 2015), or by fluid-assisted diffusion of Zr into baddeleyite and finally zircon exsolution lamellae along pre-existing crystal defects (Pape et al., 2016). The exsolved zircon lamellae and granules documented in this study may represent a similar fluid-assisted diffusive process, over a longer duration, in which all of exsolved baddeleyite is extensively converted to zircon. However there is no evidence for Zr diffusion profiles over ~25μm as observed by Pape et al. (2016); and the observed flat Zr profiles may be more indicative of widespread CDR of rutile and zircon. Further Si required to exsolve >1 wt% Zr as zircon may originate from adjacent silicate minerals. It cannot be determined, however, if Si diffusion from the rutile grain supplements zircon crystallisation due to the comprehensive resetting of several rutile trace elements in these samples.

Whilst most recent studies of UHT metamorphic rutile (Pape et al., 2016), lack comparable evidence for rutile and zircon dissolution-reprecipitation on cooling, this process is consistent with several petrological features of the Mt Charles rutiles. BSE images of rutile from sample 49688 display core domains without exsolved zircon needles (Fig. 8d), and exhibit internal compositional variation and darker rim zones (Fig. 8b). Zircon is often nucleated along pre-existing defects, orientated with {100} and {110} rutile cleavage planes (Fig. 9a). Abundant recrystallized zircon granules, rinds and lamellae are observed across samples in qz-fsp dominated domains, both leading to cracks in rutile and in recrystallized zircon. A volume change of up to +6.3% within rutile due to zircon precipitation equivalent to an additional 21996ppm Zr (0.0003 %/ppm; Table 2), documented here as a cause of cracks in rutile grains containing zircon granules (Figure 8b, d).

In cases where zircon recrystallized from rutile can be directly correlated petrologically or chemically with a rutile grain based on zircon trace element analysis, then it is possible to accurately reintegrate the Zr-in-rutile concentration ‘lost’ from a rutile. This study calculates additional Zr-in-rutile concentrations of up to 21996ppm on such reintegration. An increase of Zr-in-rutile concentration of this magnitude leads to revised

maximum metamorphic temperatures of up to 1149°C at 11kbar (Tomkins et al., 2007), compared to the apparent temperatures of 606-650°C (214-383ppm measured by in-situ SIMS, Fig. 9b). Pape et al. (2016) have already used in-situ Zr-in-rutile thermometry and zircon re-integration to infer UHT conditions up to ~ 1150°C in the Ivrea Zone in the Southern Alps. Zr-in-rutile thermometry studies in established UHT terranes (e.g. Jiao et al., 2011; Meyer et al., 2011) may require upward revisions of peak metamorphic temperature as a result.

Systematic variation in rutile and zircon petrography has characterised rutile preserving prograde, peak and post peak Zr-in-rutile signatures in anhydrous UHT pelites (Pape et al., 2016). Rutile in sample 49688 has a complex texturally controlled relationship with zircon dependent on adjacent phases, hydrated domains and subsequent fluid-rock interaction. Widespread, homogenous Zr-in-rutile resetting and presence of several habits of zircon associated with single rutile grains indicates that rutile petrography cannot be applied to characterise discrete prograde, peak and post peak metamorphic Zr-in-rutile concentrations in this case. Instead, consistent zircon-rutile petrographic relationships reflect sustained dissolution-reprecipitation and related Zr-in-rutile resetting on cooling coupled with texturally controlled fluid interaction. This phenomenon highlights the importance of considering the petrological micro-domain occupied by rutile and its potential contact with mobile fluids when interpreting rutile trace element signatures. Successful re-integration of zircon technique to evaluate the maximum peak metamorphic rutile temperatures depends on the preservation and careful imaging of zircon granules in fluid-altered domains.

The timing of Zr-in-rutile loss and resetting with zircon dissolution and reprecipitation in principle can be constrained by U-Pb dating of rutiles (dependent on U concentration) and recrystallized zircon precipitates (dependent on requirements for analytical volumes and zircon grain size). Trace element concentrations measured by zircon analyses may also help identify if those zircons are associated with Zr dissolution-reprecipitation from rutile or originate from another source. This is an exciting area for further research and development of further quantitative microanalysis from nano-SIMS instruments.

CONCLUSIONS

1. The peak P-T conditions of the Napier Complex at Mt Charles approached 1100^{o}C at 14kbar, from P-T pseudosection modelling of peak grt-sil-qz-rt, grt-spl-pl-crn-ilm assemblages in garnet bearing granulites and Zr-in-rutile temperatures across samples after zircon re-integration into rutile. A P-T path involving near-isobaric cooling (IBC) and moderate (~3kbar) decompression to 11kbar with cooling to 800-820^{o}C followed the UHT event. This high-pressure P-T path was responsible for the near-peak formation of chromium-bearing kyanite in a chromite-rutile quartzite at Mt Charles. The overall near UHT-IBC P-T path resulting in elevated pressures even after cooling through some 300^{o}C is similar in form to those reported by Hollis and Harley (2002) for the UHT part of the Napier Complex but incompatible with the UHT-ITD path at >930^{o}C recently invoked for Priestley Peak by Shimizu et al. (2013).

2. Further deep-level cooling from 800-850^{o}C to ~600-650^{o}C is recorded by partial preservation of a bt-liq-pl-kfs-ky-qz-ru±chr equilibrium assemblage, ~40 vol% mica growth in hydrated domains, and reset Zr-in-rutile temperatures 600-780^{o}C in sample 49688. Hydration of a garnet-absent, kyanite-bearing assemblage to finally produce abundant fuchsite occurred either during post-peak IBC through the crystallisation of local melt or after cooling to 800-850^{o}C and down to temperatures of ~ 720^{o}C as recorded by reset Zr-in-rutile thermometry.

3. Metamorphic fluid infiltration into the kyanite-chromium-rutile bearing sample led to the alteration of rutile, dissolution of rutile-associated zircon granules and relative depletion of Nb in rutile in hydrated fuchsite-dominated textural domains. The mobility of Zr and Nb dissolution at 600-740^{o}C indicates that the infiltrating fluid was most likely saline. Cooling to 600-750^{o}C and fluid interaction at these temperatures could have occurred as early as ca.2440Ma (Harley, 2016), or ca. 2380-2200Ma (Choi et al., 2006; Kelly and Harley, 2007; Suzuki et al., 2006). Alternately, the fuchsite-forming hydration episode may represent metasomatism as late as the Palaeozoic (Carson and Ague, 2008). Further evidence for saline fluid infiltration and related isotopic resetting (e.g. Horie et al., 2012) is required to differentiate between the two hypotheses.

4. The recovery of UHT conditions in the Napier Complex via the Zr-in-rutile thermometer is dependent on zircon re-integration and how well its limitations are overcome. Uncertainty from clustering of zircon granules and preferred precipitation in rutile cracks and grain boundaries may be reduced by numerous analyses of rutile images to recover statistically robust re-integrated Zr-in-rutile concentrations. Difficulties in differentiating between rutile-associated zircon and primary zircon inclusions may be overcome in future by analysis of zircon trace elements at micro or nano-scale (e.g. nano-SIMS). The preservation and successful imaging of zircon grains is further dependent on the petrological domain occupied by rutile and its interaction with fluid, and so requires detailed in-situ petrographic observation.

5. The Zr-in-rutile record of UHT conditions at Mt Charles is facilitated by detailed petrography and systematic trace element analysis. Taking the limitations into consideration, identification of reprecipitated zircon related to rutile and re-integration of the Zr-in-rutile concentrations (up to 2.17wt%) 'lost' by dissolution-reprecipitation allows the recovery of UHT Zr-in-rutile temperatures in the range 965-1149^{o}C, despite reset Zr-in-rutile temperatures 600-750^{o}C across all analysed samples. These recovered temperatures ~1150^{o}C are similar to the UHT conditions recorded in the Ivrea-Verbano zone using Zr-in-rutile re-integration (Pape et al., 2016). Application of zircon-reintegration may lead to revised predictions for the maximum peak temperature recorded by Zr-in-rutile thermometry studies in UHT terranes over a range of thermal durations (e.g. Jiao et al., 2011; Meyer et al., 2011).

ACKNOWLEDGEMENTS

Samples were collected from Mt. Charles, Enderby Land, Antarctica by S.L. Harley during the 1979 Australian National Antarctica Research Expedition (ANARE). We would like to thank D. Waters and an anonymous reviewer for their insightful reviews which greatly improved the quality of the manuscript, and M. Scambelluri for his careful editorial work. In addition, Nicola Cayzer, Nic Odling, Chris Hayward, Richard Hinton and John Craven of the School of Geosciences, University of Edinburgh and the Edinburgh Materials and Micro-Analysis Centre (EMMAC) are thanked for their invaluable advice on analytical techniques.

REFERENCES

Barth, M.G., McDonough, W.F., Rudnick, R.L., 2000. Tracking the budget of Nb and Ta in the continental crust. Chemical Geology 165(3-4), 197-213.

Benisek, A., Dachs, E., Kroll, H. A ternary feldspar-mixing model based on calorimetric data: development and application. Contributions to Mineralogy and Petrology 160, 327-337.

Black, L.P., James, P.R., Harley, S., 1983. The geochronology, structure and metamorphism of early Archean rocks at Fyfe Hills, Enderby Land, Antarctica. Precambrian Research 21, 197-222.

Black, L.P., Williams, I.S., Compston, W., 1986. Four zircon ages from one rock: the history of a 3930-Ma-old granulite from Mount Sones, Enderby Land, Antarctica. Contributions to Mineralogy and Petrology 94, 427-437.

Brown, M., 2006. Duality of thermal regimes is the distinctive characteristic of plate tectonics since the Neoarchean. Geology 34(11), 961-964.

Brown, M., 2007. Metamorphic conditions in orogenic belts: a record of secular change. International Geology Review 49, 193–234.

Carson, C.J., Ague, J.J., Grove, M., Coath, C.D., Harrison, T.M., 2002. U-Pb isotopic behaviour of zircon during upper-amphibolite facies fluid infiltration in the Napier Complex, east Antarctica. Earth and Planetary Science Letters 199, 287-310.

Carson, C.J., Ague, J.J., 2008. Early Palaeozoic metasomatism of the Archean Napier Complex, East Antarctica. Geological Society, London, Special Publications 308, 283-316.

Chardon, D., Gapais, D. & Cagnard, F., 2009. Flow of ultra-hot orogens: A view from the Phanerozoic. Tectonophysics 477, 105-118.

Chardon, D., Jayananda, M. & Peucat, J.-J., 2011. Lateral constrictional flow of hot orogenic crust. Insights from the Neoarchean of south India, geological and geophysical applications for orogenic plateaux. Geochemistry, Geophysics, Geosystems 12(2), 1-24.

Cherniak, D.J., Manchester, J., Watson, E.B., 2007. Zr and Hf diffusion in rutile. Earth and Planetary Science Letters 261(1-2), 267-279.

Choi, S.H., Mukasa, S.B., Andronikov, A.V., Osanai, Y., Harley, S., Kelly, N.M., 2006. Lu-Hf systematics of the earliest crust in Antarctica: The ultra-high temperature (UHT) Napier Metamorphic Complex of Enderby Land. Earth and Planetary Science Letters 246, 305-316.

Clark, C., Fitzsimons, I.C.W., Healy, D., Harley, S.L., 2011. How does the continental crust get really hot? Elements 7, 233–238.

Clark, C., Healy, D., Johnson, T., Collins, A.S., Taylor, R.J., Santosh, M. Timms, N.E., 2015. Hot orogens and supercontinent amalgamation: A Gondwanan example from southern India. Gondwana Research 28(4), 1310-1328.

Connolly, J., Petrini, K., 2002. An automated strategy for calculation of phase diagram sections and retrieval of rock properties as a function of physical conditions. Journal of Metamorphic Geology 20 697-708.

Ellis, D.J., 1980. Osumilite-sapphirine-quartz granulites from Enderby Land, Antarctica - P-T conditions of metamorphism, implications for garnet-cordierite equilibria and the evolution of the deep crust. Contributions to Mineralogy and Petrology 74, 201-210.

Ewing, T.A., Hermann, J., Rubatto, D., 2013. The robustness of the Zr-in-rutile and Ti-in-zircon thermometers during high-temperature metamorphism (Ivrea-Verbano Zone, northern Italy). Contributions to Mineralogy and Petrology 165, 757-779.

Ferry, J.M., Watson, E.B., 2007. New thermodynamic models and revised calibrations for the Ti-in-zircon and Zr-in-rutile thermometers. Contributions to Mineralogy and Petrology 154 (4), 429-437.

Hensen, B., Motoyoshi, Y., 1992. Osumilite-producting reactions in high temperature granulites from the Napier Complex, East Antarctica: Tectonic implications. Yoshida, Y., et al. (eds), Recent Progress in Antarctica Earth Science, 87-92.

Harley, S.L., 1985. Garnet-Orthopyroxene Bearing Granulites from Enderby Land, Antarctica. Metamorphic Pressure-Temperature-Time Evolution of the Archean Napier Complex. Journal of Petrology 26(4), 819-856.

Harley, S.L., 1987. A pyroxene-bearing meta-ironstone and other pyroxene-granulites from Tonagh Island, Enderby Land, Antarctica: further evidence for very high temperature (>980^{o}C) Archean regional metamorphism in the Napier Complex. Journal of Metamorphic Geology 5, 341-356.

Harley, S.L., 1989. The origins of granulites: a metamorphic perspective. Geology Magazine 126, 215-247.

Harley, S.L., 1998. On the occurrence and characterisation of ultrahigh-temperature crustal metamorphism. Geological Society, London, Special Publications 138, 81-107.

Harley, S.L., 2004. Extending our understanding of Ultrahigh temperature crustal metamorphism. Journal of Mineralogical and Petrological Sciences 99, 140-158.

Harley, S.L., 2016. A matter of time: The importance of the duration of UHT metamorphism. Journal of Mineralogical and Petrological Sciences 111, 50-72.

Harley, S.L., Hensen, B.J., 1990. Archean and Proterozoic high-grade terranes of East Antarctica (40-80°E): a case study of diversity in granulite facies metamorphism, in: Ashworth, J.R., Brown, M. (eds.) High-temperature Metamorphism and Crustal Anatexis. The Mineralogical Society Series, 320-370.

Harley, S.L., Hensen, B.J., Sheraton, J.W., 1990. Two-stage decompression in orthopyroxene-sillimanite granulites from Forefinger Point, Enderby Land, Antarctica: implications for the evolution of the Archean Napier Complex. Journal of Metamorphic Geology 8, 591-613.

Harley, S.L., Kelly, N.M., Möller, A., 2007. Zircon Behaviour and the Thermal Histories of Mountain Chains. Elements 3(1), 25-30.

Harley, S.L., Motoyoshi, Y., 2000. Al zoning in orthopyroxene in a sapphirine quartzite: evidence for >1,120°C UHT metamorphism in the Napier Complex, Antarctica, and implications for the entropy of sapphirine. Contributions to Mineralogy and Petrology 138, 293-307.

Hayden, L.A., Watson, E.B., 2007. Rutile saturation in hydrous siliceous melts and its bearing on Ti-thermometry of quartz and zircon. Earth and Planetary Science Letters 258(3-4), 561-568.

Hokada, T., 2001. Feldspar thermometry in ultrahigh-temperature metamorphic rocks: Evidence of crustal metamorphism attaining ~1100°C in the Archean Napier Complex, East Antarctica. American Mineralogist 86 (7-8), 932-938.

Hokada, T., Motoyoshi, Y. Suzuki, S., Ishikawa, M., Ishizuka, H., 2008. Geodynamic evolution of Mt Riiser-Larsen, Napier Complex, East Antarctica, with reference to the UHT mineral associations and their reaction relations. Geological Society, London, Special Publications 308, 253-282.

Hokada, T., Osanai, Y., Toyoshima, T., Owada, M., Tsunogae, T., Crowe, W.A., 1999. Petrology and metamorphism of sapphirine-bearing aluminous gneisses from Tonagh Island in the Napier Complex, East Antarctica. Polar Geoscience 12, 49-72.

Holland, T., Powell, R., 1998. An internally consistent thermodynamic data set for phases of petrological interest. Journal of Metamorphic Petrology 16(3), 309-343.

Holland, T., Powell, R., 2011. An improved and extended internally consistent thermodynamic dataset for phases of petrological interest, involving a new equation of state for solids. Journal of Metamorphic Geology 42, 673-683.

Hollis, J.A., Harley, S., 2002. New evidence for the peak temperatures and the near-peak pressure-temperature evolution of the Napier Complex. In: Ganble, J.A., Skinner, D.N.B., Henrys, S., Lynch, R. (eds). Antarctica at the Close of a Millenium. Proceedings Volume, 8th International Symposium on Antarctic Earth Science. Royal Society of New Zealand Bulletin 35, 19-29.

Horie, H., Hokada, T., Hiroi, Y., Motoyoshi, Y., Shiraishi, K., 2012. Contrasting Archean crustal records in western part of the Napier Complex, East Antarctica: New constraints from SHRIMP geochronology. Gondwana Research 21, 829-837.

Jamieson, R.A., Beaumont, C., Warren, C.J., Nguyen, M.H., 2010. The Grenville Orogen explained? Applications and limitations of integrating numerical models with geological and geophysical data. Canadian Journal of Earth Sciences 47, 517-539.

Jamieson, R.A., Beaumont, C., 2011. Coeval thrusting and extension during lower crustal ductile flow – implications for exhumation of high-grade metamorphic rocks. Journal of Metamorphic Geology 29, 33-51.

Jamieson, R.A., Beaumont, C., 2013. On the origin of orogens. Geological Society of America Bulletin 125, 1671-1702.

Jiao, S., Guo, J., Mao, Q., Zhao, R., 2011. Application of Zr-in-rutile thermometry: a case study from ultrahigh-temperature granulites of the Khondalite belt, North China Craton. Contributions to Mineralogy and Petrology 162, 379, 393.

John, T., Klemd, R., Klemme, S., Pfander, J.A., Hoffman, J.E., Gao, J., 2011. Nb-Ta fractionation by partial melting at the titanite-rutile transition. Contributions to Mineralogy and Petrology 161, 35-45.

Kelly, N., Harley, S., 2005. An integrated microtextural and chemical approach to zircon geochronology: refining the Archean history of the Napier Complex, east Antarctica. Contributions to Mineralogy Petrology 149, 57-84.

Kelsey, D., 2008. On ultrahigh-temperature crustal metamorphism. Gondwana Research (13), 1-29.

Kelsey, D., Hand, M., 2015. On Ultrahigh temperature crustal metamorphism: Phase equilibria, trace element thermometry, bulk composition, heat sources, timescales and tectonic settings. Geoscience Frontiers 6, 311-356.

Kelsey, D., Powell, R., 2011. Progress in liking accessory mineral growth and brakdown to major mineral evolution in metamorphic rocks: a thermodynamic approach in the Na2O-CaO-K2O-FeO-MgO-Al2O3-SiO2-H2O-TiO2-ZrO2 system. Journal of Metamorphic Geology 21, 559-578.

Kelsey, D.E., White, R.W., Holland, T.J.B., Powell, R., 2004. Calculated phase equilibrium in K_2O-FeO-MgO-Al_2O_3-SiO_2-H_2O for sapphirine-quartz bearing mineral assemblages. Journal of Metamorphic Geology 22(6), 559-578.

Kooijman, E., Smit, M.A., Mezger, K., Berndt, J., 2012. Trace element systematics in granulite facies rutile: implications for Zr geothermometry and provenance studies. Journal of Metamorphic Geology 30(4), 397-412.

Korhonen F.J., Clark, C., Brown, M., Bhattacharya, S., Taylor, R., 2013. How long-lived is ultrahigh temperature (UHT) metamorphism? Constraints from zircon and monazite geochronology in the Eastern Ghats orogenic belt, India. Precambrian Research 234, 322-350.

Korhonen, F.J., Saw, A.K., Clark, C., Brown, M., Bhattacharya, S., 2011. New constraints on UHT metamorphism in the Eastern Ghats Province through the application of phase equilibria modelling and in situ geochronology. Gondwana Research 20(4), 764-781.

Liu, S.J., Li, J.H., Santosh, M., 2010. First application of the revised Ti-in-zircon geothermometer to Paleoproterozoic ultrahigh-temperature granulites of Tuguiwula, Inner Mongolia, North China Craton. Contributions to Mineralogy and Petrology 159, 225-235.

Luvizotto, G.L., Zack, T., 2009. Nb and Zr behaviour in rutile during high-grade metamorphism and retrogression: An example from the Ivrea-Verbano Zone. Chemical Geology 261(3-4), 303-317.

Meyer, M., Timm, J., Brandt, S., Klemd, R., 2011. Trace element composition of rutile and the application of Zr-in-rutile thermometry to UHT metamorphism (Epupa complex, NW Namibia). Lithos 126(3-4), 388-401.

Motoyoshi, Y., Hensen, B., 1989. Sapphirine-quartz-orthopyroxene symplectites after cordierite in the Archean Napier Complex, Antarctica: evidence for a counterclockwise P-T path? European Journal of Mineralogy 1(3), 467-472.

Newton, R.C., 1990. Fluids and shear zones in the deep crust. Tectonophysics 182(1-2), 21-37.

Osanai, Y., Owada, M., Kamei, A., Hamamoto, T., Kagami, H., Toyoshima, T., Nakano, N., Nam, T.N., 2006. The Higo metamorphic complex in Kyushu, Japan as the fragment of Permo-Triassic metamorphic complexes in East Asia. Gondwana Research 9(1-2), 152-166.

Pape, J., Mezger, K., Robyr, M., 2016. A systematic evaluation of the Zr-in-rutile thermometer in ultra-high temperature (UHT) rocks. Contributions to Mineralogy and Petrology 171(44), doi: 10.1007/s00410-016-1254-8.

Piazolo, S., La Fontaine, A., Trimby, P., Harley, S., Yang, L., Armstrong, R., Cairney, J.M., 2016. Deformation-induced trace element redistribution in zircon revealed using atom probe tomography. Nature Communications 7; 10490, doi: 10.1038/ncomms10490.

Pownall, J.M., Hall, R., Armstrong, R.A., Forster, M.A., 2014. Earth's youngest known ultrahigh-temperature granulites discovered on Seram, eastern Indonesia. Geology 42(4), 279-282.

Rapp, J.F., Klemme, S., Butler, I.B., Harley, S.L., 2009. Extremely high solubility of rutile in chloride and fluoride-bearing metamorphic fluids: An experimental investigation. Geology 38(4) 323-326.

Rubatto, D., Hermann, J., 2007. Experimental zircon/melt and zircon/garnet trace element partitioning and implications for the geochronology of crustal rocks. Chemical Geology 241(1-2), 38-61.

Sandiford, M., Powell, R., Pyroxene exsolution in granulites from Fyfe Hills, Enderby Land, Antarctica: evidence for 1000^{o}C metamorphic temperatures in Archean continental crust. American Mineralogist 71, 946-954.

Santosh, M., Liu, S.J., Tsonogae, T., Li, J.H., 2012. Paleoproterozoic ultrahigh-temperature granulites in the North China Craton: Implications for tectonic models on extreme crustal metamorphism. Precambrian Research 222-223, 76-106.

Sawyer, E.W., 1994. Melt segregation in the continental crust. Geology 22(11), 1019-1022.

Sawyer, E.W., 1999. Criteria for the recognition of partial melting. Physics and Chemistry of the Earth, Part A: Solid Earth and Geodesy 24(3), 269-279.

Seifert, F., Langer, K., 1970. Stability Relations of Chromium Kyanite at High Pressures and Temperatures. Contributions to Mineralogy and Petrology 28, 9-18.

Sheraton, J.W., Tingey, R.J., Black, L.P., Offe, L.A., Ellis, D.J., 1987. Geology of an unusual Precambrian high-grade metamorphic terrane – Enderby Land and Western Kemp Land, Antarctica. Australian Bureau of Mineral Resources, Geology and Geophysics, Bulletin 223.

Shimizu, H., Tsunogae, T. & Santosh, M., 2013. Petrology and phase equilibriium modelling of sapphirine + quartz assemblage from the Napier Complex, East Antarctica: Diagnostic evidence for Neoarchean ultrahigh-temperature metamorphism. Geoscience Frontiers 4, 655-666.

Sizova, E., Gerya, T., Brown, M., Perchuk, L.L., 2010. Subduction styles in the Precambrian: Insight from numerical experiments. Lithos 11(3-4), 209-229.

Sizova, E., Gerya, T., Brown, M., 2014. Contrasting styles of Phanerozoic and Precambrian continental collision. Gondwana Research 25(2), 522-545.

Smyth, J.R., McCormick, T.C., 1995. Crystallographic data for minerals. Mineral Physics and Crystallography, A handbook of Physical Constants, AGU (1995).

Stepanov, A.S., Hermann, J., Fractionation of Nb and Ta by biotite and phengite: Implications for the "missing Nb paradox". Geology 41(3), 303-306.

Stuwe, K., 1995. Thermal buffering effects at the solidus. Implications for the equilibration of partially melted metamorphic rocks. Tectonophysics 248, 39-51.

Suzuki, S., Arima, M., Williams, I.S., Shiraishi, K., Kagami, H., 2006. Thermal history of the UHT metamorphism in the Napier Complex, East Antarctica: insights from zircon, monazite and garnet ages. Journal of geology 114, 65-84.

Suzuki, S., Kagami, H., Ishizuka, H., Hokada, T., 2001. Sm-Na mineral isochron age of sapphirine-quartz gneiss from the Mt. Riiser-Larsen area in the Napier Complex, East Antarctica. Polar Geoscience 14, 88-98.

Tajcmanova, L., Connolly, J.A.D., Cesare, B., 2009. A thermodynamic model for titanium and ferric iron solution in biotite. Journal of Metamorphic Geology 27, 153-165.

Taylor, R.J.M., Harley, S.L., Hinton, R.W., Elphick, S., Clark, C., Kelly, N.M., 2015. Experimental determination of REE partition coefficients between zircon, garnet and melt: a key to understanding high-T crustal processes. Journal of Metamorphic Geology 33, 231-248.

Taylor-Jones, K., Powell, R., 2010. The stability of sapphirine + quartz: calculated phase equilibria in FeO-MgO-Al_2O_3-SiO_2-TiO_2-O. Journal of Metamorphic Geology 28(6), 615-633.

Taylor-Jones, K., Powell, R., 2015. Interpreting zirconium-in-rutile thermometric results. Journal of Metamorphic Geology 33(2), 115-122.

Timms, N.E., Kinny, P.D., Reddy, S.M., Evans, K., Clark, C., Healy, D., 2011. Relationship among titanium, rare earth elements, U-Pb ages and deformation microstructures in zircon: Implications for Ti-in-zircon thermometry. Chemical Geology 280(1-2), 33-46.

Tomkins, H.S., Powell, R., Ellis, D.J., 2007. The pressure dependence of the zirconium-in-rutile thermometer. Journal of Metamorphic Geology 25, 703-713.

Touret, J.L.R., Santosh, M., Huizenga, J.M., 2016. High-temperature granulites and supercontinents. Geoscience Frontiers 7(1), 101-113.

Touret, J.L.R., Huizenga, J.M., 2012. Fluid-assisted granulite metamorphism: A continental journey. Gondwana Research 21(1), 224-235.

Tsunogae, T., Santosh, M., Osanai, Y., Owada, M., Toyoshima, T., Hokada, T., 2002. Very high-density carbonic fluid inclusions in sapphirine-bearing granulites from Tonagh Island in the Archean Napier Complex, East Antarctica: implications for CO_2 infiltration during ultrahigh-temperature (T>1,100^{o}C) metamorphism. Contributions to Mineralogy and Petrology 143(3), 273-299.

Tsunogae, T., Santosh, M., Dubessy, J., Osanai, Y., Owada, M., Hokada, T., Toyoshima, T., 2008. Carbonic fluids in ultrahigh-temperature metamorphism: evidence from Raman spectroscopic study of fluid inclusions

in granulites from the Napier Complex, East Antarctica. Geological Society, London, Special Publications 308, 317-332.

Vernon, R.H., 1999. Quartz and feldspar microstructures in metamorphic rocks. The Canadian Mineralogist 27, 513-524.

Vernon, R.H., 2011. Microstructures of melt-bearing regional metamorphic rocks. GSA memoirs 207, 1-11.

Vila, M., Fernandez, M. Jimenez-Munt, I., 2010. Radiogenic heat production variability of some common lithological groups and its significance to lithospheric thermal modelling. Tectonophysics 490, 152-164.

White, R.W., Powell, R., Clarke, G.L., 2002. The interpretation of reaction textures in Fe-rich metapelitic granulites of the Musgrave Block, central Australia: Constraints from mineral equilibra calculations in the system K_2O-FeO-MgO-Al_2O_3-SiO_2-H_2O-TiO_2-Fe_2O_3. Journal of Metamorphic Geology 20, 41-55.

White, R.W., Powell, R., Holland, T.J.B., 2007. Progress relating to calculation of partial melting equilibria for metapelites. Journal of Metamorphic Geology 25(5), 511-527.

Whitney, D.L., Evans, B.W., 2010. Abbreviations for names of rock-forming minerals. American Mineralogist 95, 185-187.

Fig. 1: Map and satellite images of the Napier Complex, Enderby Land, Antarctica. A: Overall outline of Antarctica and terrane map of Enderby Land after Sheraton et al. (1987) and Hokada and Harley (2004); showing the Archean Napier, Proterozoic-Palaeozoic Rayner and Early Palaeozoic Lutzlow-Holm complexes. Fig. 1b inset. B: Satellite image of the UHT zone of the Napier complex, including the pressure dependent grt+osu = als+opx+kfs mineral isograd observed by Harley and Hensen (1990). CH - Mt Charles, RL – Mt Riiser-Larsen, TI – Tonagh Island, PP – Priestley Peak, C – Mt Cronus, H – Mt Hardy, CB – Casey Bay. C: Satellite image of Mt Charles, sampled locations inset.

Fig.2: The Zr-in-rutile and Ti-in-zircon thermometry records for the UHT Napier Complex (Harley, 2016). Zr-in-rutile records are reset to <775^{o}C, with a population between 600-650^{o}C recorded by this study (Table 1). By contrast, Ti-in-zircon frequently records near-peak metamorphic temperatures >850^{o}C at specified localities in the Napier Complex.

Fig. 3: Photomicrographs of garnet bearing samples 49677 and 49702. A: 49677; Porphyroblastic garnet and sillimanite with a ribbon quartz matrix. B: 49677: garnet, sillimanite porphyroblasts with euhedral accessory rutile associated with grt. C: 49702; large ~1cm grt porphyroblasts with multi-stage fluid, quartz, rutile, spinel, zircon inclusions. Mantled by sil porphyroblasts, rutile and ribbon quartz. D: 49677; Porphyroblastic garnet and rutile. E: 49677; grt porphyroblast with ribbon quartz and euhedral associated rutile. F: 49702; garnet porphyroblasts mantled by sillimanite clusters. Sillimanite, garnet and rutile occur in ribbon quartz.

Fig. 4: BSE images of rutile in sample 49677. A: 677-ru2; Euhedral rutiles occur adjacent to garnet and are internally homogenous, and are associated with low volumes of recrystallized zircon, minor rutile recrystallization along garnet grain margins. B: 677-ru3; Euhedral rutile in ribbon quartz fabric. Large proportional volume of zircon recrystallization. Cracks in rutile from volume change. Rounded and elongate zircon granules are recrystallized on grain boundaries.

Fig. 5: Photograph, photomicrographs and BSE image of sample 49701. A: thin section of 49701, notice abundant ~40% vol garnet, interstitial spinel and mesoperthite and feldspathic, quartz absent domains. B: Primary and secondary grt (grt1, grt2). Spinel, ilmenite and corundum are present in various petrological domains, rutile (701-ru1) is associated with grt2. Widespread granoblastic mesoperthite domains dominate the quartz absent assemblage. C: Rutile and sillimanite occur in synchronous late stage growth with grt2. D: porphyroblastic primary garnet with spinel and late stage rutile intergrowths. E: BSE image of Grt1 porphyroblast showing a grt2 growth with interstitial plagioclase – preserving a k-feldspar absent peak assemblage (Fig. 6b).

Fig. 6: P-T pseudosections for representative bulk rock compositions of garnet-bearing granulites 49701 and 49677, with Xpy and Xgrs garnet composition isopleths. A: 49677 grt-sil-bt-qz-rt granulite; liq-grt-sil-qz-rt peak assemblage and stability fields are constrained by garnet Xgrs = 0.14 and XMg = 0.53-0.54 are highlighted B: 49701 gt-sp-crn-sil-fsp-rt granulite. Stability fields from petrological observations and garnet

chemistry are highlighted; a liq-pl-spl-grt-ilm-crn peak assemblage and Xgrs values 0.050-0.060 suggest a high-P 14kbar, 1100^{o}C peak assemblage while late stage sillimanite stability and Xpy 0.340-0.345 constraining later conditions of ~850^{o}C, 11kbar. C: Overall P-T evolution with fields from stability fields are highlighted in Fig. 6a (blue) and Fig. 6b (yellow). Resultant inferred, near UHT-IBC path with moderate decompression is displayed. Detailed interpretation presented in text.

Fig. 7: Photograph, photomicrographs and BSE image of sample 49688. A: thin section of sample 49688, notice well banded mica and quartz bearing domains and ~40vol% mica. B: Altered kyanite porphyroblast in a mica domain with associated biotite, biotite inclusions. Quartz and feldspar display low angle grain boundaries (indicating partial melt presence), skeletal chromite intergrown with fuchsite mica. C: Mature ribbon quartz texture, heavily intergrown with rutile needles. Fluid inclusions are present in some zones. Curved qz-fsp grain boundaries indicate the presence of partial melt. D: Rutile (688ru-1, 3, 4) in mica and quartz-feldspar domains with accessory pyrite. Rutile in contact with mica is rounded, euhedral rt preserved in qz. E: BSE image showing curviplanar quartz-feldspar grain boundaries and interstitial mica domains.

Fig. 8: BSE images of rutiles in sample 49688. A,B: 688-ru5; Euhedral rutile in quartz-dominated domain is partially exposed to mica domian. Rod shaped recrystallised zircon inclusions and rounded zircon along grain boundaries are observed. Associated chr occurs where ru is exposed to the mica-dominated domain. C,D: 688-ru6; Euhedral ru set in a quartz-feldspar dominated domain. Recrystalised zircon needles and rod inclusions are >20µm in diameter. Intra-grain cracks occur due to a volume change on zircon recrystallisation. Rounded inclusions on grain boundary. E,F: 688-ru9; rounded rutile in mica domain. Low volume of associated recrystallised zircon, low volume change, associated chr.

Fig. 9: A: Crystal habits of zircon recrystallisation in rutile. Rod inclusions and precipitates are localised along {100} and {110} cleavage in perfect tetrahedral rutile. Volume change occurs due to recrystallized zrn due to the higher molar volume of zircon and the resultant intra-grain rutile cracks. Granular exsolution along rutile grain boundaries and in rutile cracks is caused by the volume increase. B: In situ rutile trace element trends and Zr-in-rutile thermometry with temperatures from zircon re-integration. Petrological sketches of rutile grains show adjacent phases and the in-situ location of SIMS and EPMA point and line analyses. EPMA line analyses of rutile trace elements with Zr-in-rutile thermometry and Nb/Ta ratios are displayed. (i) Sample 49677, (ii) Sample 49702, (iii) Sample 49688. Detailed discussion in text.

Fig. 10. A: Nb/Ta ratios for all samples (SIMS and EPMA data). Best-fit Nb/Ta ratio = 13.34 across all samples; a sub-chondritic signature. B: Nb-Ta populations as given by mica and quartz-feldspar domain rutiles in sample 49688. Rutiles in qz-fsp domains plot a cluster around 1950ppm at a large range of Nb/Ta ratios, while mica domain rutiles have depleted Nb concentrations of ~1000ppm over a smaller range of Nb/Ta. A strong fractionation to a small range of Nb/Ta and Nb concentrations fluid mediated mica domains. Detailed discussion in text.

Fig. 11: T-X(MH_2O) pseudosection plots between representative bulk rock compositions for anhydrous X0 (H_2O mol% = 0) and hydrous X1 (H_20 mol% = 15) bulk-rock compositions at 11kbar for ky-fu-fsp-qz-chr-rt granulite sample 49688. A: T-X(MH_2O) plot showing stable mineral assemblages across T-X conditions. B: T-X(MH_2O) plot with kyanite vol % contours. C: T-X(MH_2O) plot with mica vol % contours. D: T-X(MH_2O) plot with melt vol% contours. E: Three T-MH_2O evolutions (i), (ii) and (iii) between peak and reset conditions defined by Zr-in-rutile thermometry (Table 1, 2) and a relict bt-liq-pl-kfs-ky-rt equilibrium assemblage (see text). Note injection of metamorphic H_2O at 725-750^oC occurs at $MH_2O > 0.6$. F: Petrological sketches of textures observed in sample 49688 quartz-feldspar and mica dominated domains at (i) bt-liq-pl-kfs-ky-qz-rt equilibria and (ii) hydration of feldspar domains at $MH_2O > 0.6$, <820^oC. For rutile petrological behaviour in quartz/mica domains see Fig. 8. Detailed interpretation in text.

Fig. 12: A: Overall metamorphic evolution of Mt Charles samples. Long lived UHT-near IBC is constrained by pseudosection modelling of garnet bearing samples 49677 and 49701. H_2O addition during IBC is constrained by T-M(H_2O) modelling of sample 49688 (Figure 11). Fluid-rock interaction leads to a depleted Nb-Ta signature, altered rutile and dissolved zircon in sample 49688 (Figure 8, 10). The reset Zr-in-rutile field is constrained by in-situ SIMS and EPMA analyses across all samples. Re-integrated Zr-in-rutile field constrained by zircon re-integration method across all samples. See **Metamorphic evolution of Mt Charles granulites** for detailed discussion. The P-T path is not necessarily continuous. B: P-T paths in the Napier complex as constrained by: (i) this study, (ii) Harley (1985, 1998), (iii, iv) Shimizu et al. (2013) and (v) Harley et al. (1990).

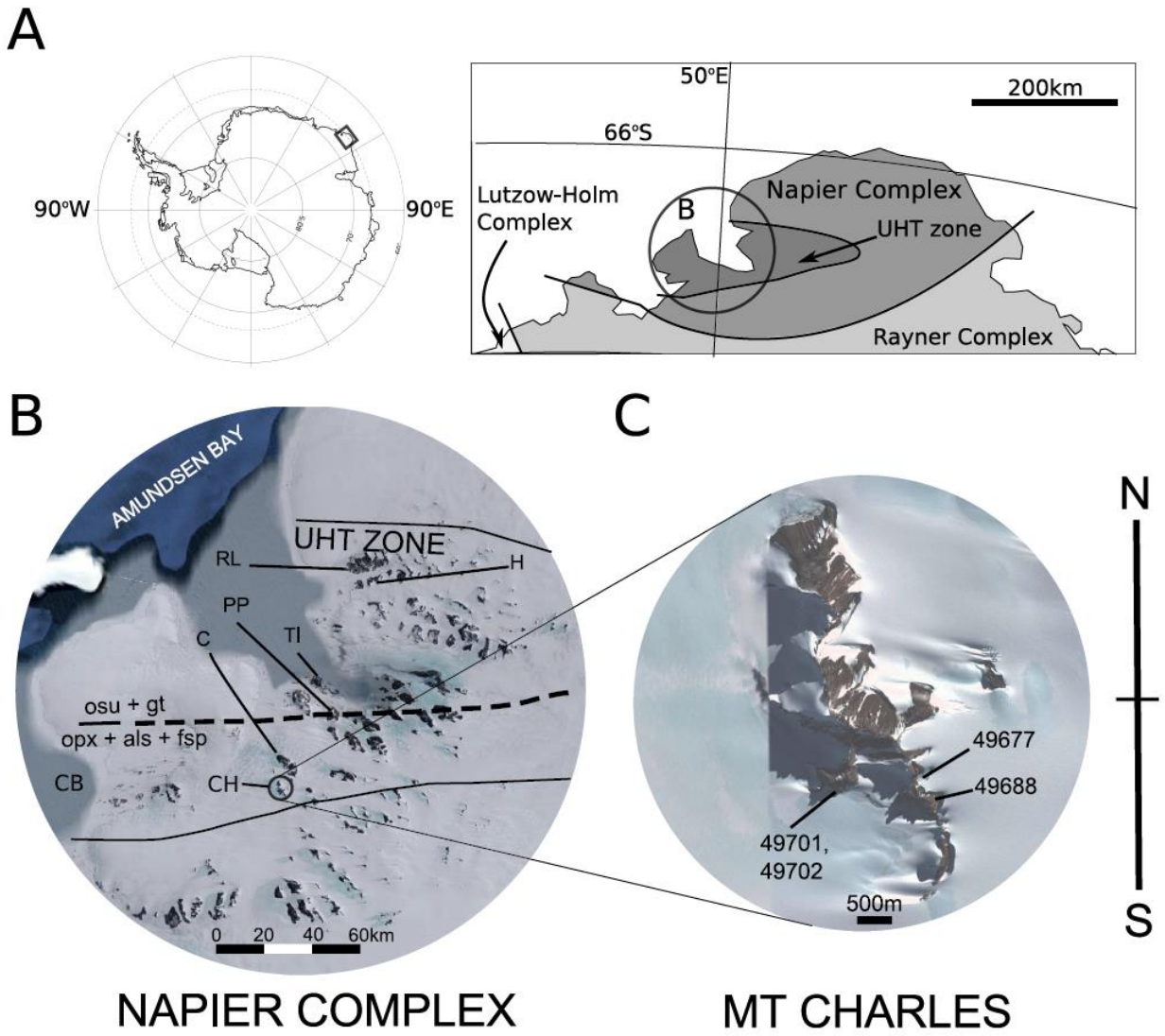

Figure 1

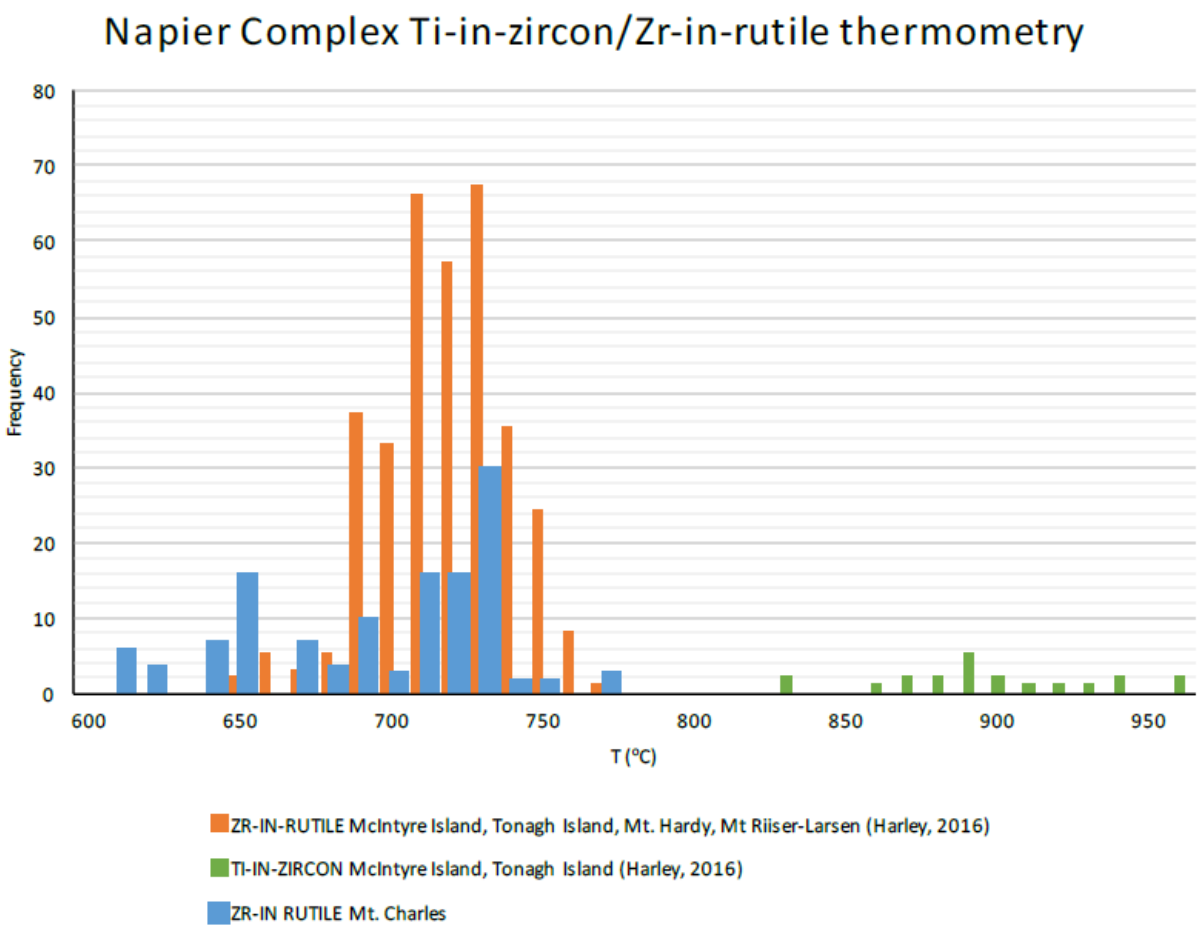

Figure 2

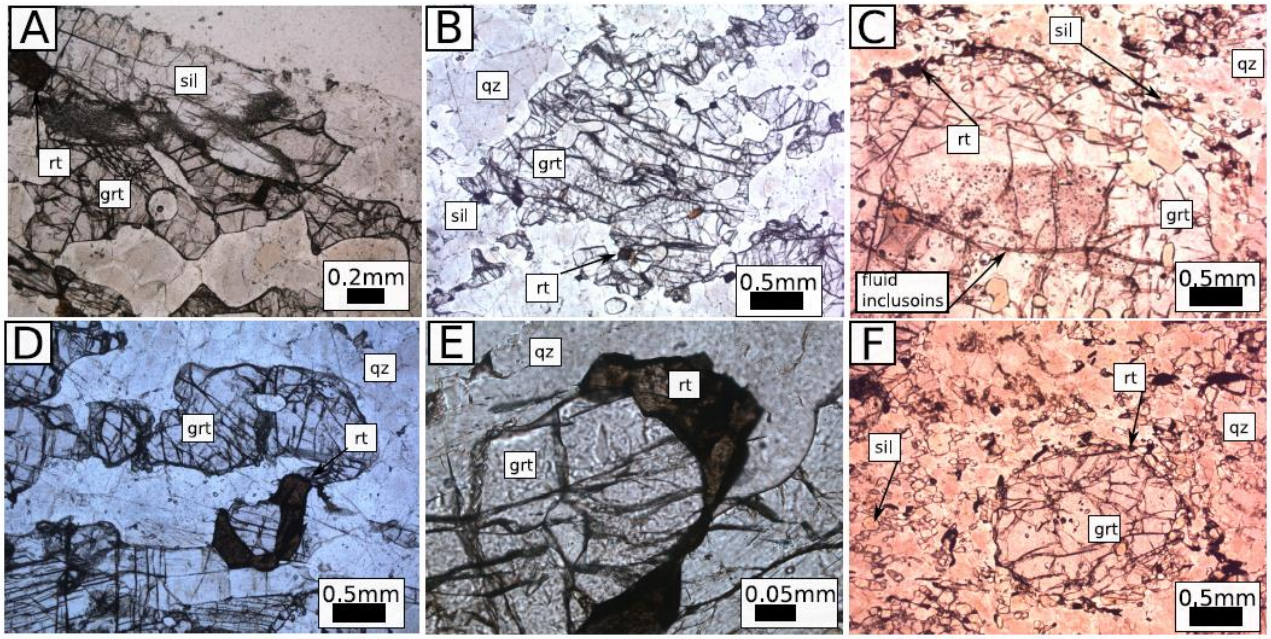

Figure 3

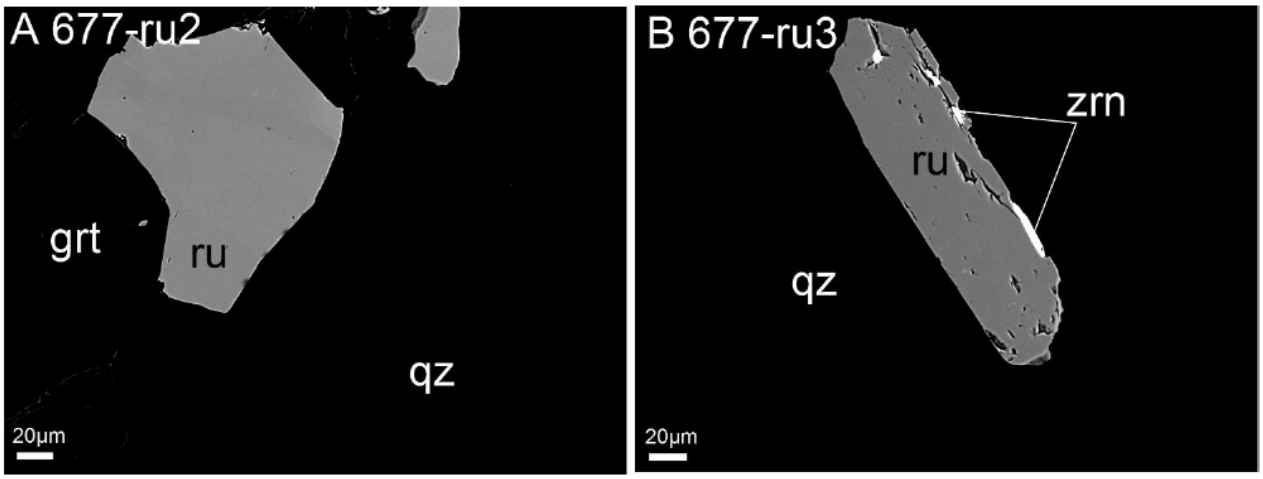

Figure 4

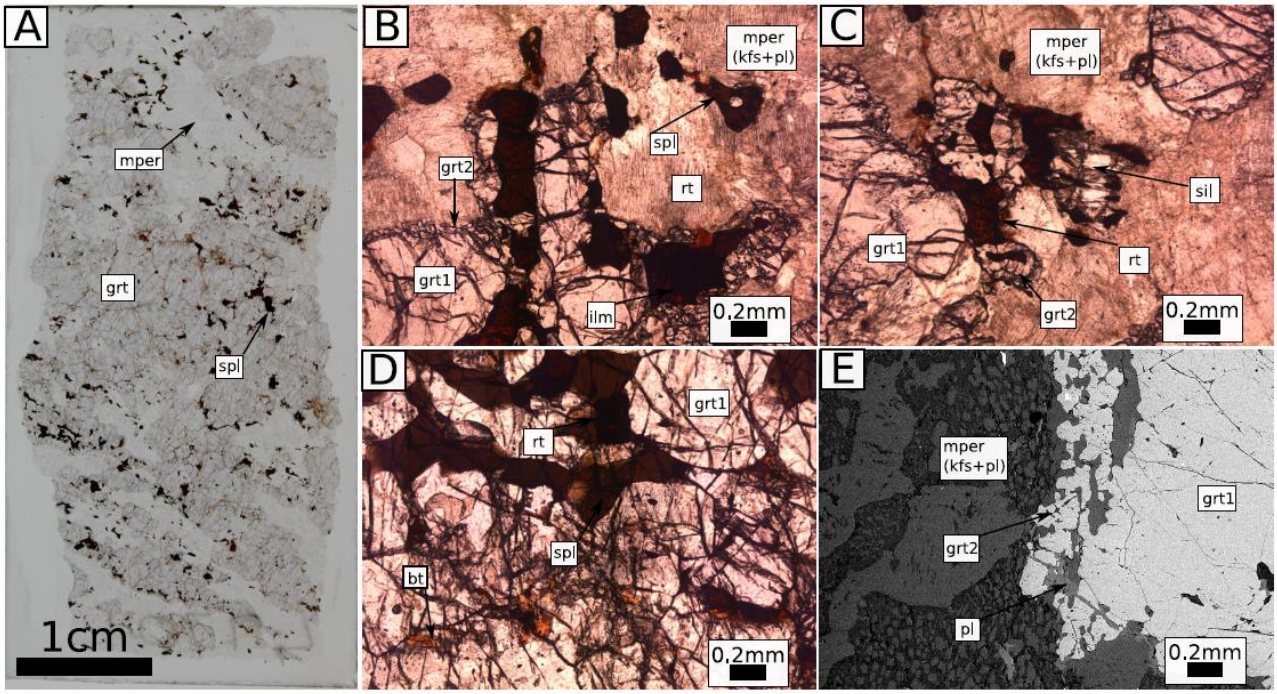

Figure 5

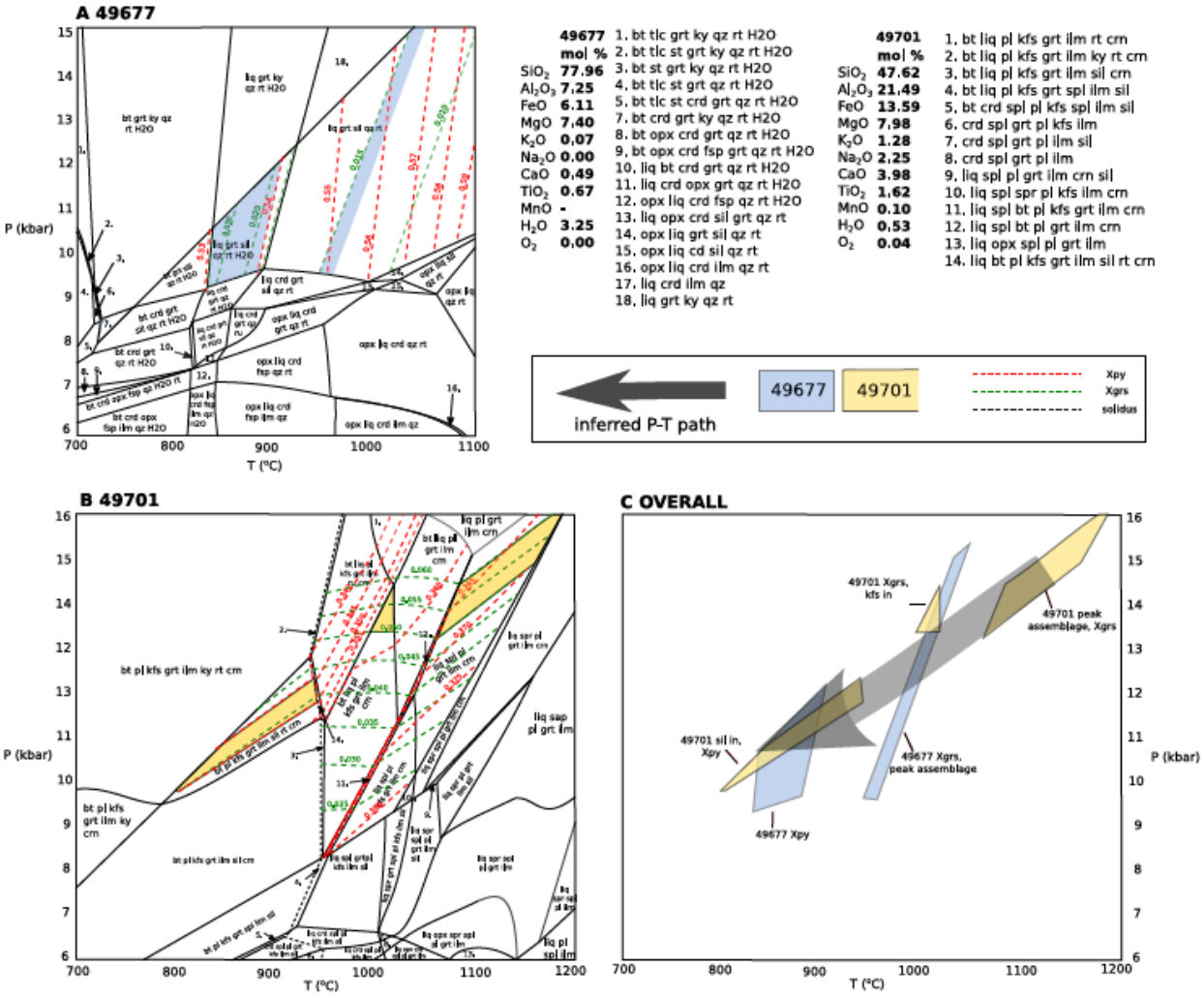

Figure 6

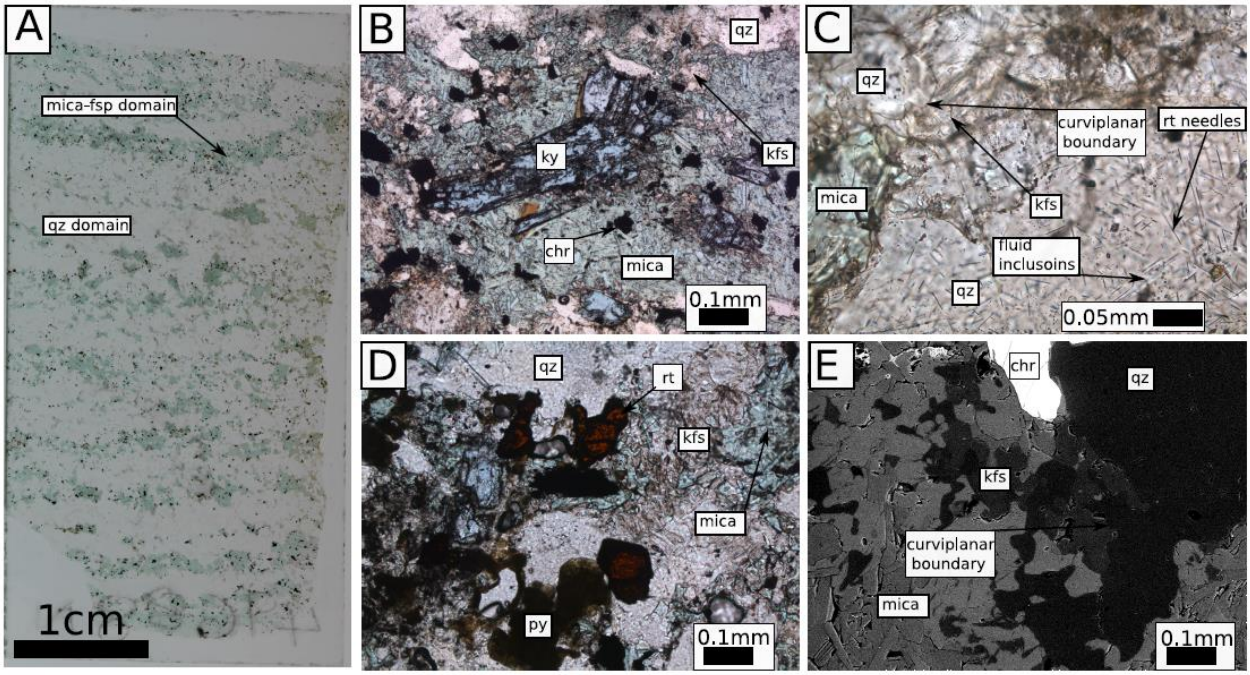

Figure 7

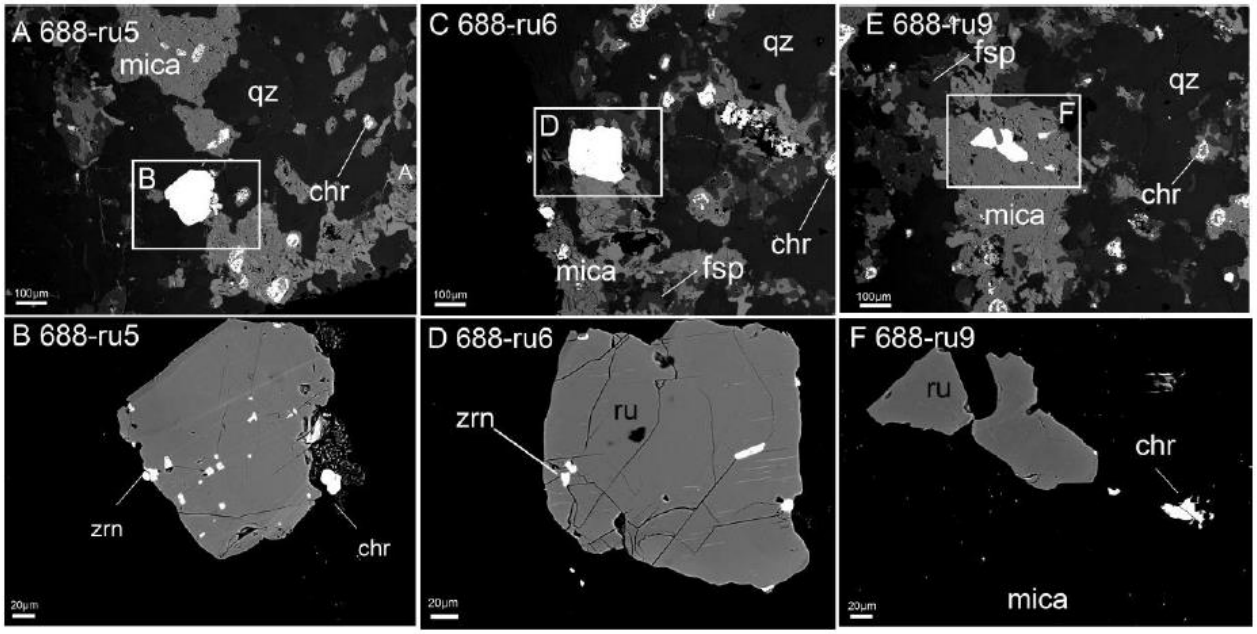

Figure 8

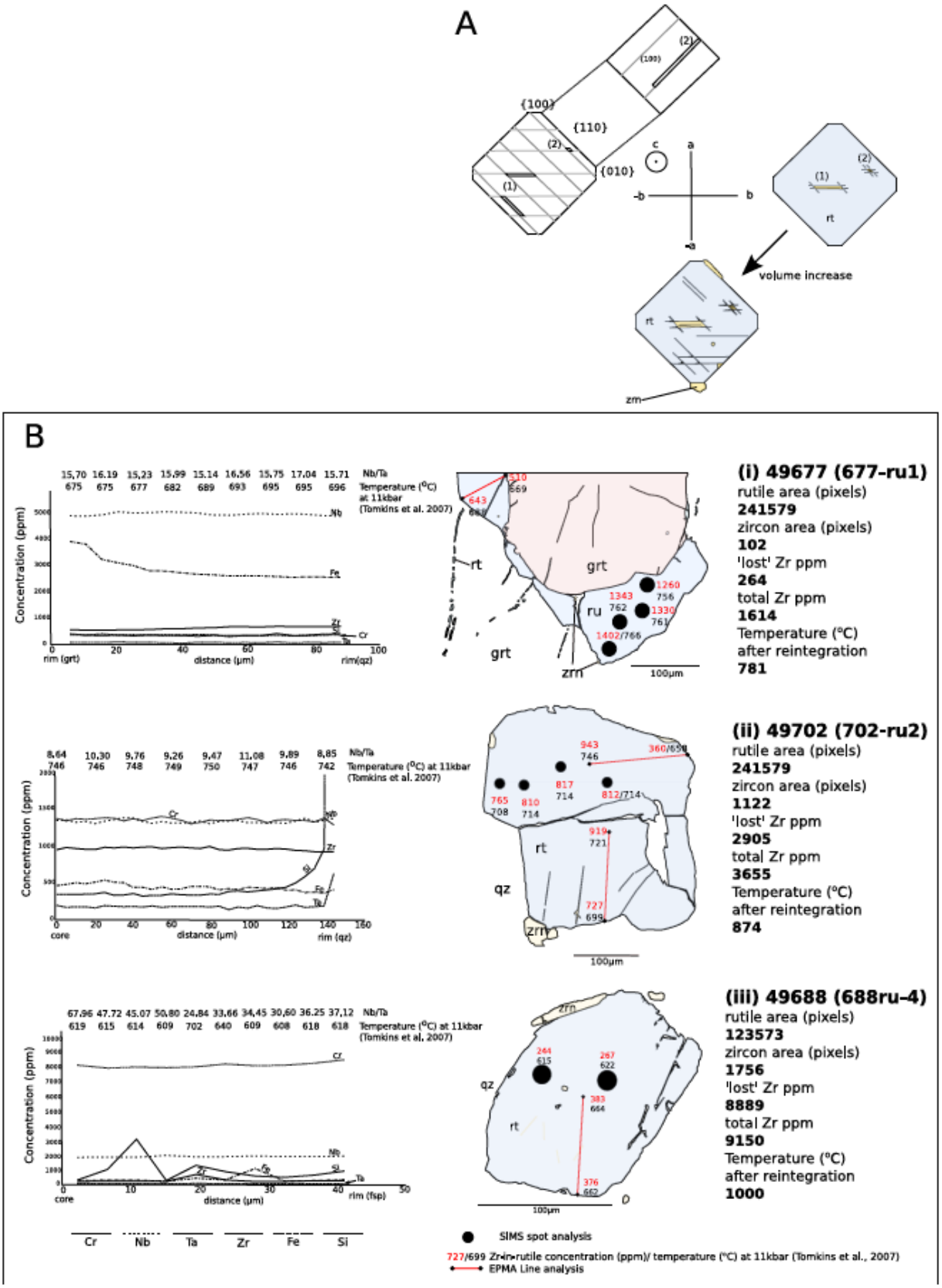

Figure 9

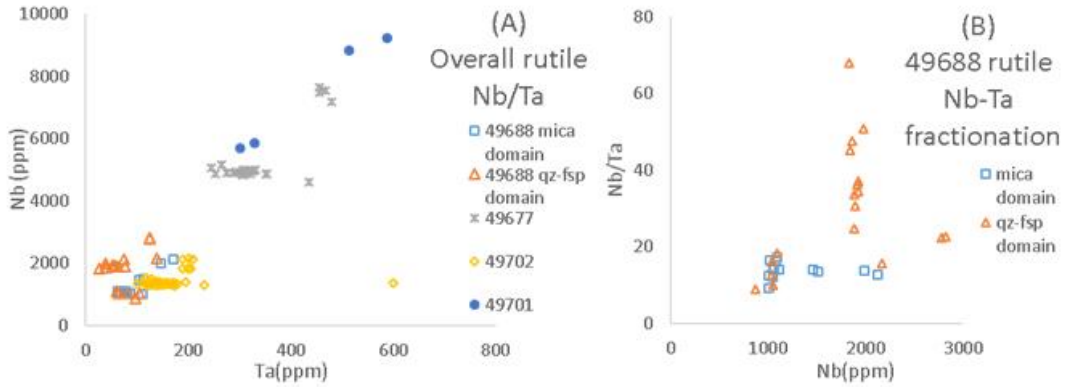

Figure 10

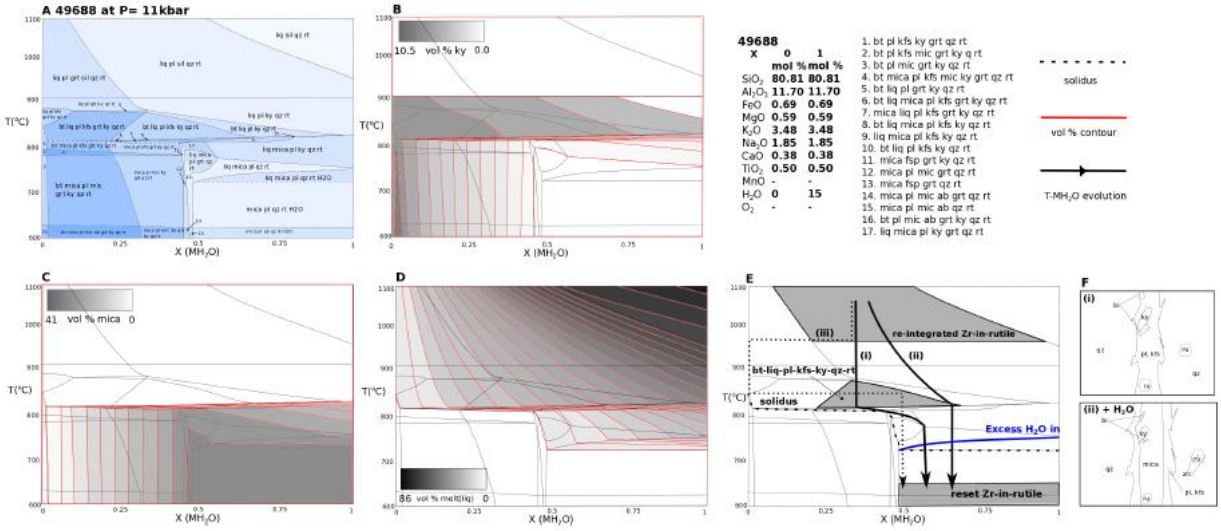

Figure 11

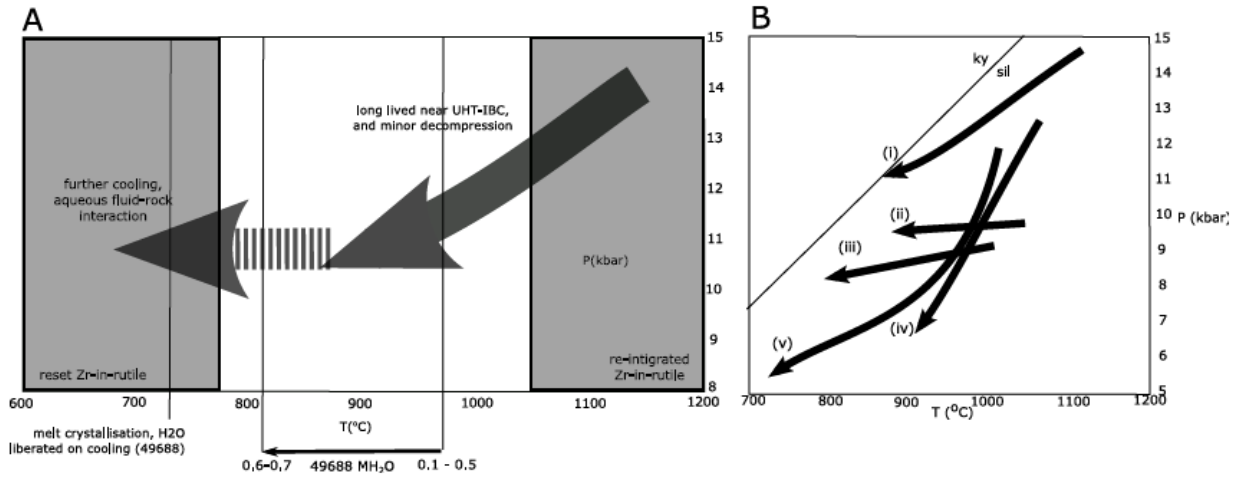

Figure 12

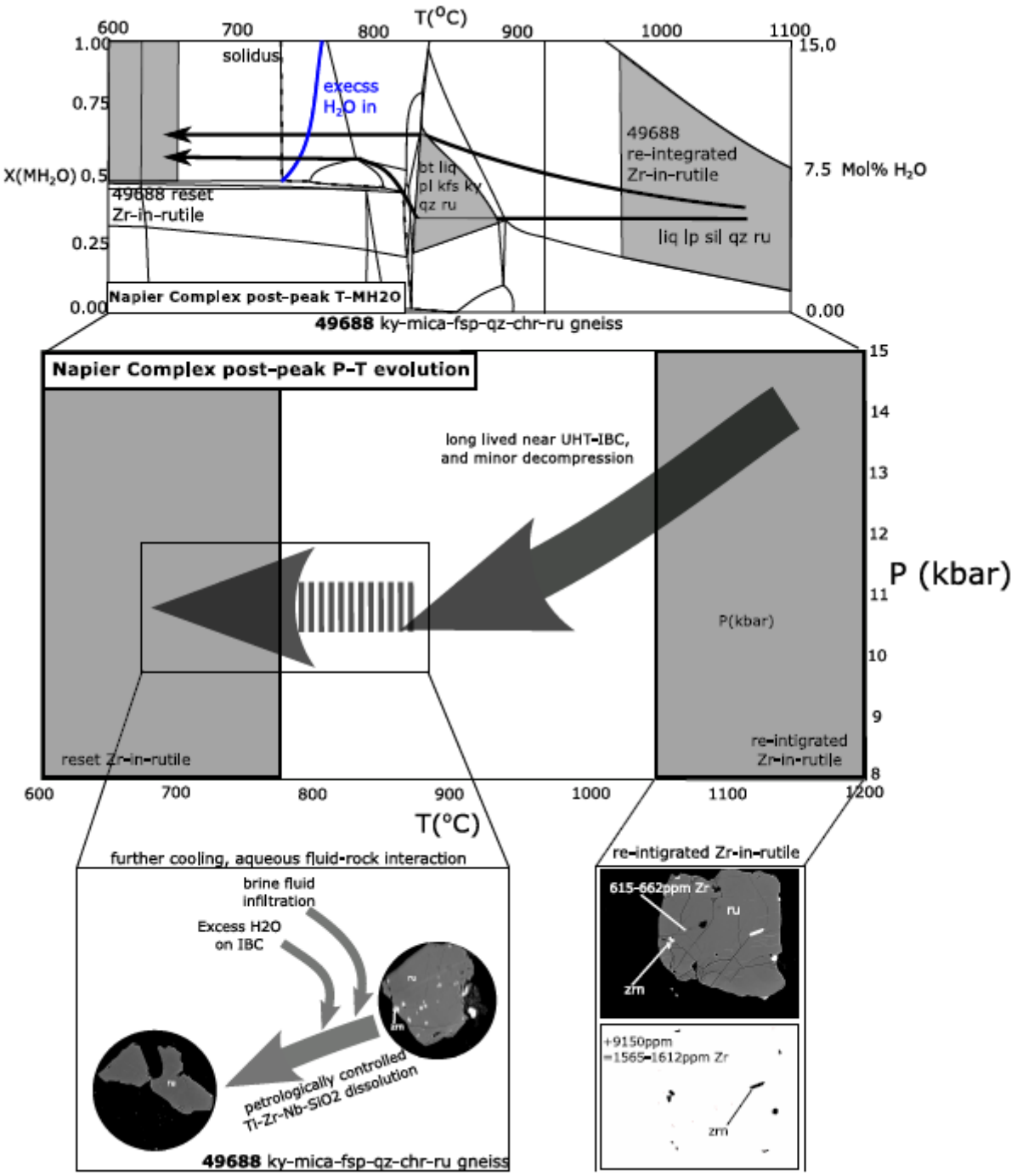

Graphical abstract

RUTILE (SIMS)	49677				49688								49701		49702						
Rutile Nr	677-ru1				688-ru1		688-ru2		688-ru3		688-ru4		701-ru1		702-ru1			702-ru2			
	core	rim (qz)	rim (grt)	core	core	rim	core	rim	core	rim	core	rim	core	rim	core	rim (grt)	rim (qz)	core	rim	mid	core
Mg (ppm)	6.16	5.37	8.89	6.82	4.90	3.24	2.63	3.54	4.03	4.64	2.99	3.68	1.48	1.72	8.29	7.68	6.87	2.60	2.12	3.28	3.00
Al	304.29	304.35	307.53	305.94	49.72	63.97	41.10	43.96	45.33	217.07	54.41	110.12	76.68	72.80	170.43	130.73	232.07	114.51	113.57	115.20	117.52
Si	45.80	29.60	43.40	37.10	34.40	46.30	20.20	20.10	31.70	387.00	33.50	148.00	23.00	19.90	135.50	233.70	187.10	21.70	17.90	20.80	28.40
Ca	7.22	1.10	1.97	1.05	16.15	21.77	5.32	4.99	3.73	3.46	5.08	17.74	2.94	0.00	37.90	29.97	12.49	15.45	8.23	11.29	1.78
Ti	589980	590350	589780	590930	589730	589410	591380	592980	590160	591740	590120	591370	589360	590330	590090	590010	589970	589070	589950	589900	590500
V	917.65	924.95	917.74	907.54	1539.60	1523.90	1698.30	1661.10	1631.80	1715.00	1635.70	2018.30	5088.50	5261.40	3696.10	3688.60	3753.70	2577.50	2580.00	2572.30	2606.00
Cr	15.98	16.35	14.97	15.64	8418.90	8111.10	8041.40	8359.60	8388.10	9314.10	7944.30	8476.20	3424.30	3372.00	1246.40	1244.20	1266.00	1438.70	1453.80	1438.00	1468.40
Fe	3590.90	3601.20	3507.90	3565.90	1108.40	1256.70	269.01	130.99	1064.90	243.95	583.01	383.85	253.10	-7.65	566.66	682.75	485.44	662.24	614.19	653.56	546.12
Mn	2.84	1.80	2.60	2.45	2.80	2.44	2.22	1.81	1.95	1.87	2.09	1.87	1.22	0.63	3.00	2.13	2.42	2.79	2.10	2.92	2.76
Y	0.07	0.08	0.31	0.08	0.05	0.04	0.01	0.03	0.03	0.02	0.11	0.51	0.07	0.03	0.05	0.07	0.08	0.04	0.03	0.04	0.04
Zr	1343	1402	1260	1330	219	236	301	311	253	306	267	244	910	730	249	244	254	817	765	812	810
Nb	7541.30	7636.10	7167.30	7482.70	2781.70	2825.30	1464.80	1514.70	2173.50	2139.70	2131.80	1991.20	8833.60	9226.90	2135.30	2170.30	2121.50	1837.70	1827.00	1845.50	1835.90
Ti+Ti	4698.70	4679.70	4589.60	4578.10	2373.10	2491.70	2529.40	2754.30	2583.50	2587.40	2519.30	2521.40	3388.00	3108.30	2574.00	2606.50	2606.90	3267.30	3288.70	3362.60	3330.80
Ba	2.46	2.07	3.06	2.54	1.63	1.38	1.22	1.47	1.08	5.71	1.46	1.43	1.60	1.47	2.52	1.96	1.88	1.73	1.58	2.14	1.93
La	0.53	0.42	0.56	0.49	0.19	0.20	0.14	0.09	0.11	0.45	0.38	2.05	0.72	0.70	0.82	1.48	0.58	0.13	0.11	0.13	0.21
Ce	0.43	0.69	0.70	0.77	0.28	0.35	0.10	0.25	0.29	0.36	0.42	3.16	0.72	0.61	0.90	2.21	1.00	0.23	0.26	0.28	0.30
Sm	0.02	0.13	0.58	0.13	0.14	0.00	0.02	0.00	0.00	0.00	0.00	0.28	0.00	0.00	0.00	0.25	0.23	0.00	0.00	0.00	0.00
Ho	0.00	0.00	-0.01	0.00	0.00	0.00	0.00	0.00	0.00	0.00	0.00	0.04	0.00	0.00	0.00	0.00	0.00	0.00	0.00	0.00	0.00
Ta	468.13	455.25	480.19	455.45	123.84	125.40	105.37	112.09	138.36	73.51	170.40	146.03	513.86	589.08	208.90	200.50	189.50	203.94	189.23	199.93	198.90
ZR-IN-RUTILE THERMOMETRY (TOMKINS ET AL., 2007)																					
Pressure (kbar)	11	11	11	11	11	11	11	11	11	11	11	11	11	11	11	11	11	11	11	11	11
T(K)	1035	1039	1029	1034	880	885	903	906	890	905	895	888	997	977	889	888	891	987	981	987	987
T(^{o}C)	762	766	756	761	607	612	630	633	617	632	622	615	724	704	616	615	618	714	708	714	714

Table 1: In-situ SIMS trace element analyses and Zr-in-rutile temperatures at 11kbar (Tomkins et al., 2007) for samples 49677, 49688, 49701, 49702. For spatial distribution of analyses in selected rutile grains see figure 7 and supplementary information. Complimentary EPMA trace element data, rutile BSE images can be found in supplementary information.

*Table 2: Zr-in-rutile re-integration method (see **Methods**). To be cross-referenced with rutile petrography (Figures 4, 6, 7) and quantitative Zr-in-rutile trace element data (Table 1). Total Zr ppm denotes addition of Zr ppm from 'lost' recrystallized zircon with suitable quantitative SIMS analysis values. Zr-in-rutile thermometry at 11kbar using Tomkins et al., 2007 calibration.*

Zircon re-integration	**49677**			**49688**							**49702**	
Rutile Nr	677-ru1	677-ru2	677-ru3	688-ru1	688-ru4	688-ru5	688-ru6	688-ru7	688-ru8	688-ru9	702-ru2	702-ru1
adjacent phases	Grt-qz	Grt-qz	qz	Qz-mica	Qz-mica	Qz	Qz	Qz-mica	Mica	Mica	Qz	Grt-qz
Ru area	241579	496879	328126	115413	123573	745381	1290810	330243	334644	334515	106396	241579
$ZrSiO_4$ area	102	619	7810	1541	1756	25900	15911	3450	447	91	1107	1122
Ru mol	11226	23089	15247	5363	5742	34637	59982	15346	15550	15544	4944	11226
Zrn mol	3	16	199	39	45	660	405	88	11	2	28	29
Ru wt	896941	1844825	1218275	428508	458805	2767469	4792552	1226135	1242475	1241996	395030	896941
Zrn wt	476	2889	36455	7193	8196	120893	74268	16104	2086	425	5167	5237
ZR-IN-RUTILE CONCENTRATION												
Zr wt	218	1322	16682	3579	4078	60150	36951	8012	1038	211	2571	2606
Zr ppm	243	717	13693	8352	8889	21735	7710	6535	836	170	6508	2905
Total Zr ppm	1593	978	13954	8653	9150	21996	7971	6796	1097	431	7258	3655
Volume change (%)	0.08	0.23	4.34	2.44	2.59	6.34	2.25	1.91	0.24	0.05	1.90	0.85
ZR-IN-RUTILE THERMOMETRY (TOMKINS ET AL., 2007)												
Pressure (kbar)	11	11	11	11	11	11	11	11	11	11	11	11
T(K)	1053	1004	1341	1264	1273	1422	1252	1229	1015	932	1238	1147
T(^{o}C)	780	731	1068	991	1000	1149	979	956	742	659	965	874

Highlights

- Peak ultra-high temperatures (UHT) >1100^{o}C at11-14kbar in the Napier Complex.
- Post-peak evolution dominated by cooling and minor decompression to 850^{o}C, 11kbar.
- Petrographic record of hydrous fluid-rock interaction during cooling below ~820^{o}C.
- Widespread Zr-in-rutile resetting throughout post-peak Napier Complex cooling.
- Valid Zr-in-rutile records of UHT conditions requires zircon reintegration.